



Contents lists available at ScienceDirect

Arabian Journal of Chemistry

journal homepage: www.ksu.edu.sa

Original article

Revolutionizing corrosion protection in seawater using innovative layered double hydroxide/polyvinylidene fluoride LDH@PVDF composite coatings

Jwahr M. AlGhamdi^{a,*}, Hissah A. Alqahtani^{a,*}, Nuhu Dalhat Mu'azu^b, Mukarram Zubair^b, Shamsuddeen A. Haladu^c, Mohammad Saood Manzar^b

^a Department of Chemistry, College of Science, Imam Abdulrahman Bin Faisal University, 31451 Dammam, Saudi Arabia

^b Department of Environmental Engineering, College of Engineering, Imam Abdulrahman Bin Faisal University, P.O. Box 1982, 31451 Dammam, Saudi Arabia

^c Department of Basic Engineering Sciences, College of Engineering, Imam Abdulrahman Bin Faisal University, P.O. Box 1982, 31451 Dammam, Saudi Arabia



ARTICLE INFO

Keywords:

Corrosion
Coatings
Layered compounds
Layered double hydroxide
Long-term
PVDF

ABSTRACT

This study pioneers a novel approach to achieving sustainable corrosion protection in seawater environments by incorporating layered double hydroxide (LDH) fillers into polymeric polyvinylidene fluoride (PVDF) coatings to create a corrosion-resistant coating for mild steel. LDH composites were successfully synthesized using coprecipitation and hydrothermal methods, with characterization through x-ray diffraction analysis (XRD), fourier-transform infrared spectroscopy FTIR, morphological analysis, and elemental mapping. LDH@PVDF coatings with the thickness of $40 \pm 2 \mu\text{m}$ exhibited improved surface properties, superior adhesion, hydrophobicity, and antifouling characteristics. Corrosion resistance was comprehensively assessed using open circuit potential (OCP), potentiodynamic polarization (PDP), and electrochemical impedance spectroscopy (EIS). ZLDH@PVDF coating outperformed others, demonstrating exceptional long-term corrosion protection (up to 60 days) without diffusion-controlled processes. The mechanism of corrosion protection of ZLDH@PVDF coating has been discussed.

1. Introduction

Steel alloys have been utilized extensively in a variety of industries, including machinery parts, building construction, and pipelines, due to their low cost, favorable conductivity, machinability, and weldability (Kartsonakis, 2021). Unfortunately, metal degradation or corrosion is always a pressing issue in engineering applications and industries (Anjum et al., 2019). As a result, numerous surface modification techniques, such as cathodic and anodic protection (Cheng et al., 2022), inhibition (Bakhtaoui et al., 2021; Luo et al., 2024; Vieira et al., 2022) surface treatment (Mroczkowska et al., 2021), and coatings (Online et al., 2017), have been proposed to enhance their corrosion protection property (Du et al., 2018). Among these various protective approaches, coatings have drawn increasing attention due to their excellent anticorrosion performance resulting from the superior barrier effect (Jialing Chen et al., 2019; Li et al., 2018). The primary function of the anticorrosion coating is to shield the metal from corrosive species found in various environments by providing an effective barrier (Ren et al., 2023; Zheludkevich et al., 2010). Corrosion-resistant coatings have been

developed through a variety of methods, including conversion coatings, magnetron sputtering anodizing, sol-gel synthesis, self-assembly, and polymer coatings (Iqbal and Fedel, 2019).

In recent years, various polymer-based coatings have been extensively investigated for enhanced corrosion protection (Ahmad et al., 2023; Choong et al., 2024; Sun et al., 2023). Among these, Polyvinylidene fluoride (PVDF) a semi-crystalline polymer that possesses 59.4 % fluorine by mass, exhibited promising chemical, thermal and mechanical stability, and superhydrophobic characteristics (Ali et al., 2021). PVDF is widely used as a coating to minimize corrosion, enhance wear resistance, and protect metals in corrosive environments. However, its soft surface and void volume can lead to pore formation, making it permeable to oxygen, water, and ions. This permeability increases susceptibility to substrate adhesion reduction and potential damage to superhydrophobic coatings (Qian et al., 2021). This limitation has hindered the industrial application of PVDF coatings for long-term corrosion protection. To overcome this challenge, various nano additives, including nanomaterials, carbon-based compounds, metal oxides, and others, have been incorporated into polymeric coatings to enhance their

* Corresponding authors.

E-mail addresses: jmalghamdi@iau.edu.sa (J.M. AlGhamdi), hqqahtani@iau.edu.sa (H.A. Alqahtani).

<https://doi.org/10.1016/j.arabjc.2024.105775>

Received 14 October 2023; Accepted 2 April 2024

Available online 4 April 2024

1878-5352/© 2024 Published by Elsevier B.V. on behalf of King Saud University. This is an open access article under the CC BY-NC-ND license (<http://creativecommons.org/licenses/by-nc-nd/4.0/>).

corrosion resistance characteristics (Cai et al., 2021; Mohammadkhani et al., 2020; Wen et al., 2020).

The presence of additives such as PVP (Centa and Miheř, 2022) and fnAl_2O_3 (Ghazali et al., 2023) not only reduced the wettability and penetration of water or corrosive ions but also improved the thermal/electrical conductivity and mechanical stability of the coatings [25,26]. Nano-scale composite coatings, formed by integrating 2-dimensional layered materials (2D-LMs) into the polymer matrix using surface modification and interface modulation techniques, enhance durability and barrier properties while imparting stiffness and dimensional stability characteristic of 2D-LMs. The positive effects of 2D-LMs on anti-corrosion properties, particularly LDHs, have been extensively studied, demonstrating their effectiveness for corrosion protection (Du et al., 2018; Jiang et al., 2022; Su et al., 2020).

Layered double hydroxides (LDHs) have garnered significant attention as one of the prominent layered nanofillers. Due to their unique and exceptional performances, polymer/LDH nanocomposites have become the focus of attention in the field of corrosion protection material (Mochane et al., 2020; Wen et al., 2020). The potential uses of LDHs as coatings or films to protect metals like steel (Liu et al., 2019), magnesium alloys (Junfeng Chen et al., 2019), and aluminum alloys (Liu et al., 2015) have recently been the subject of extensive research (Zhang et al., 2014). Recently, LDHs demonstrated to be potential materials for multifunctional coating systems due to versatile cationic/anionic compositions, low-toxicity, excellent barrier and ion-exchange characteristics, high surface-to-volume ratio with the capability to intercalate various species within LDH interlayers (Iqbal et al., 2020).

Generally, various polymer/LDH composites exhibit high corrosion protection performance in marine environments. For instance, Hu et al. found that a coating containing polymer–clay nanocomposites (PANI/AD-LDH) provided a more protective layer against corrosion compared to separate applications of AD-LDH and PANI (Hu et al., 2014). Additionally, Imanieh et al. synthesized MgAl-LDH incorporated with sodium molybdate to create a smart coating of PVA/LDH composites, achieving enhanced corrosion resistance through high inhibitor release rates at different pH levels (Imanieh and Afshar, 2019).

In conclusion, polymer/LDH nanocomposites have plenty of properties against corrosion despite the preparation challenges. As far as we know, PVDF/LDH composite coatings have not been investigated for corrosion applications. In this work, two types of LDH composites (MgAl-LDH and ZnAl-LDH) were synthesized using the combined method of co-precipitation method and hydrothermal crystallization. A polymeric base coating (PVDF) made use of this matrix to provide a smart or functional coating with a thickness of $40 \pm 2 \mu\text{m}$ for protecting steel alloys.

2. Materials and methods

2.1. Materials

Low carbon steel samples (AISI 1004) with dimensions ($18.5 \times 18.5 \times 2.5 \text{ mm}^3$) were used as substrates, which mainly consist of 0.178 % manganese, 0.0618 % aluminum, 0.0473 % carbon, 0.0091 % phosphor, 0.0062 % sulfur, 0.0048 % copper, 0.0118 % nickel, 0.005 silicon, and 0.0083 % chrome. Zinc (II) nitrate hexahydrate $\text{Zn}(\text{NO}_3)_2 \cdot 6\text{H}_2\text{O}$ (LOBA Chemie), magnesium (II) nitrate hexahydrate $\text{Mg}(\text{NO}_3)_2 \cdot 6\text{H}_2\text{O}$ (LOBA Chemie), aluminum (III) nitrate nonahydrate $\text{Al}(\text{NO}_3)_3 \cdot 9\text{H}_2\text{O}$ (Techno Pharmchem), sodium hydroxide NaOH (PanReac AppliChem), sodium nitrate NaNO_3 (PanReac AppliChem), Poly(vinylidene fluoride) (PVDF, average $M_w = 534,000$ by GPC, powder) (Sigma-Aldrich), N, N-Dimethylformamide (DMF, ACS reagent, $\geq 99.8\%$) (Sigma-Aldrich), and sodium chloride NaCl (LOBA Chemie) were used in this work. All the analytical grade chemicals were used as received without further purification. The deionized water was used in all the experimental processes.

2.2. Synthesis of the MLDH and ZLDH powder

The pristine LDHs $\text{Mg}_2\text{Al}_1\text{-NO}_3\text{-LDH}$ (denoted as MLDH) were synthesized using a combined co-precipitation and hydrothermal processing technique of inorganic nitrate salts. To obtain a stable layered compounds, the $\text{M}^{2+}/\text{M}^{3+}$ ratio was set at 2:1, and NO_3^- was used as the anion (Wen et al., 2020). The procedure for the synthesis adopted in this study for the Mg-Al-LDH has been described elsewhere (Liu et al., 2018). First, 0.50 M $\text{Mg}(\text{NO}_3)_2 \cdot 6\text{H}_2\text{O}$ and 0.25 M $\text{Al}(\text{NO}_3)_3 \cdot 9\text{H}_2\text{O}$ were dissolved in 50 ml of deionized water. Then the solution obtained was added dropwise to 100 ml of 1.50 M NaNO_3 solution (pre-adjusted to pH 9.5) under vigorous constant stirring using a magnetic stirrer for over 45 min while operating at room temperature. The pH of the slurry was maintained at 9.5 ± 0.5 during the synthesis by the 2 M NaOH solution. Nitrogen gas was bubbled through the slurry during the synthesis to ensure CO_2 presence was avoided. Afterwards, the resulting slurry was transferred into a Teflon-lined stainless-steel autoclave with a 200 ml capacity. The autoclave was sealed tightly and transferred into pre-heated oven at 120°C for 24 h to increase the crystallinity of the LDHs. Finally, the product was collected by centrifugation, and washed five times with deionized water until the filtrate had neutral pH to ensure that the excess of the ions was removed prior to washing with ethanol. Lastly, the white powder of MLDH composite was obtained by overnight oven drying at 60°C and grounded into fine powder ready for use. A schematic illustration of the synthesis of MLDH composite is described in Fig. 1. $\text{Zn}_2\text{Al}_1\text{-NO}_3\text{-LDH}$ (denoted as ZLDH) was synthesized using a similar procedure but using $\text{Zn}(\text{NO}_3)_2 \cdot 6\text{H}_2\text{O}$ as a starting reagent instead of $\text{Mg}(\text{NO}_3)_2 \cdot 6\text{H}_2\text{O}$.

2.3. Preparation of the anti-corrosion coatings

Prior to applying the polymeric coatings, the steel specimens underwent a polishing process using silicon carbide (SiC) paper. The polishing procedure involved progressively using different grit sizes of SiC paper, starting from 60 grit paper and advancing to 100, 180, 220, 320, 400, 600, 800, and finally, 1200-grit. This process helped achieve a mirror-like surface on the steel specimens. After polishing the samples were thoroughly cleaned with deionized water to remove any greasy dirt and then followed by drying.

For the preparation of the coatings, 2 wt% of MLDH or ZLDH composites were exfoliated in 10 ml DMF by ultrasonically irradiating for 30 min. Then, 0.8 g of PVDF was added to the exfoliated LDH layers solution and stirred with a mechanical stirrer (600 rpm) for 30 min at 40°C until the homogenous mixture was achieved. The coatings were denoted as MLDH@PVDF and ZLDH@PVDF for MLDH and ZLDH composites, respectively. Fig. 2 shows a schematic illustration of the preparation process of the anticorrosion coatings used in this work. For comparison purposes, the neat PVDF coating was prepared following the same process described earlier, but without the addition of LDH composites. The coatings were applied onto the polished mild steel substrates using the drop-casting method. Subsequently, all the coated samples were dried in an oven at 155°C for 2 h for effective curing. The abbreviations of all the samples are expressed as shown in Table 1.

2.4. Characterization

The Fourier transform infrared (FTIR) spectroscopic spectrums of samples were recorded using a SHIMADZU instrument to analyze surface functional groups and the chemical bonding of the powder samples, in the range of $4000\text{--}400 \text{ cm}^{-1}$ with a 2 cm^{-1} spectral resolution by the KBr pellet technique. The LDHs crystalline phase was investigated with X-ray diffraction (XRD) with a Shimadzu X-ray diffractometer using $\text{Cu K}\alpha$ radiation over the angle range 2θ range from 2 to 90° . Raman spectrum of the MLDH and ZLDH in the range from 300 to 1800 cm^{-1} were investigated. A scanning electron microscopy (VEGA-3, TESCAN coupled with energy dispersive spectrometer EDS detector) was used to

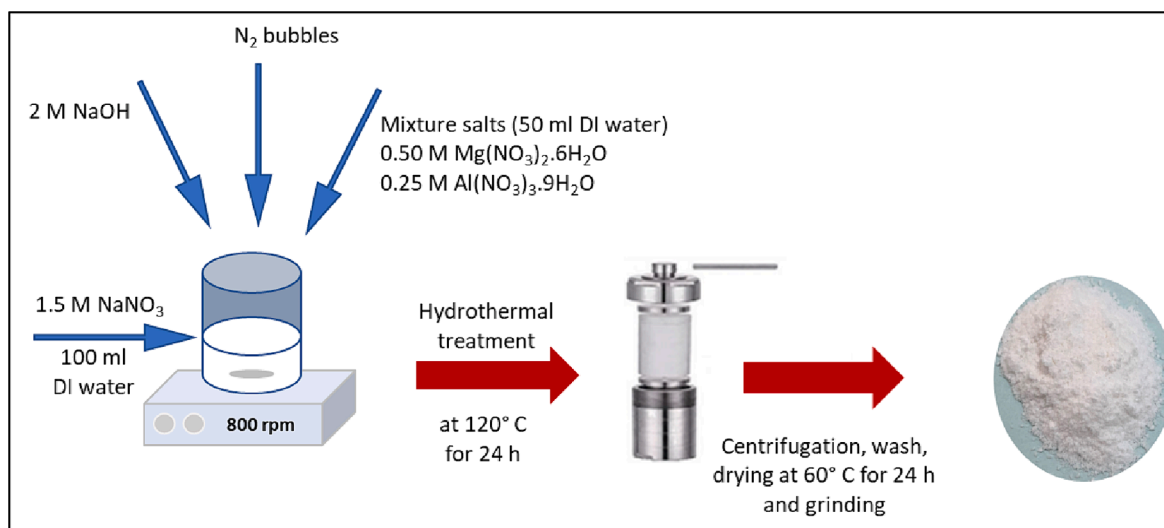


Fig. 1. A schematic diagram of synthesis MLDH.

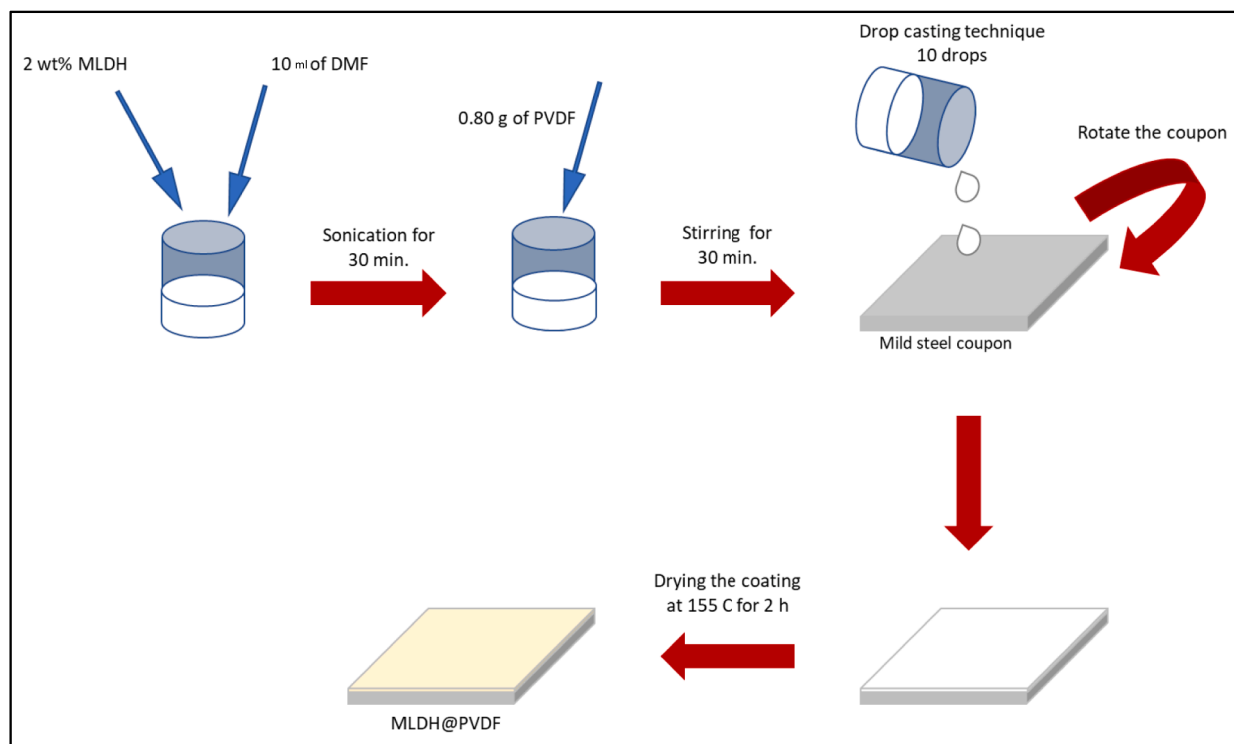


Fig. 2. A schematic illustration of MLDH@PVDF coating preparation.

Table 1

Identification of the samples with name codes.

Sample ID	Definition
Bare substrate	Uncoated mild steel sample
MLDH	Mg ₂ Al-NO ₃ -LDH powder
ZLDH	Zn ₂ Al-NO ₃ -LDH powder
Neat PVDF	Pure PVDF coating without LDH filler
MLDH@PVDF	The coating of PVDF with MLDH filler
ZLDH@PVDF	The coating of PVDF with ZLDH filler

analyze the surface and cross-sectional morphologies as well as the elemental analysis of the specimens. The surface roughness of the bare substrate and the coated samples was investigated using a 3D optical

profilometer (Profilom 3D, Germany).

The evaluation of surface wetting properties for both the coated steel samples and the uncoated substrate was conducted by measuring the static contact angle (CA) between the surface and a water droplet at 25 °C, utilizing Ginifab software. The contact angle of water was determined by placing 10 μL of deionized water droplets on the surface and capturing high-resolution optical images of the droplets using a camera with a magnifying zoom lens. This allowed us to observe the extent of the water droplet spreading on the surface of the sample. To assess coating adhesion, we employed a cross-cut tape test, which involved using a cross-cut tester equipped with 7 blades spaced at 1 mm intervals. Two sets of perpendicular cuts were made to create a grid of 36 small blocks on the coated sample. Subsequently, adhesive tape was

applied to the cross-cut area and pulled back as close to a 180° angle as possible, with cross-cut adhesion evaluated following the ASTM D3359 standard test procedure (Qian et al., 2021).

2.5. Scratch test

The surface of the coated samples was scratched with a sharp knife to form a scratch with sufficient depth to reach the substrate. The samples were immersed in a 3.5 % wt. NaCl solution for 15 days at room temperature. The evolution of the scratches on the surface was observed and analyzed by EIS spectra after 15 days.

2.6. Electrochemical characterization

The electrochemical corrosion measurements of all steel samples were performed by a Gamry electrochemical workstation (Interface 1000 E, Model 11146) in a typical three-electrode system. The corrosive electrolyte used was 3.5 % NaCl with all the measurements conducted at ambient temperature and saturated with respect to air (pH \approx 6.8). The coated steel sample with a fixed area of 1 cm² was used as the working electrode, while a saturated calomel electrode (SCE) served as the reference electrode, and a Pt sheet was used as the counter electrode. After immersing the samples in the medium, the open circuit potential (OCP) at the equilibrium state of the system was recorded with respect to SCE for at least 1 h before testing. The corrosion behavior of the coated samples was studied by means of potentiodynamic polarization curves

with respect to OCP. Tafel plots were obtained by scanning the potential from -500 to $+1000$ mV at a scan rate of 1 mV/min. The corrosion current density and other electrochemical parameters were determined by fitting tools using Gamry Echem software.

Electrochemical impedance spectroscopy (EIS) measurements of all samples were also carried out at open circuit potential in the above three-electrode setup with an amplitude of 10 mV and in the frequency range from 10^5 to 10^{-2} Hz with a step of 10 points per decade. For long-term studies, the impedance spectra were collected in various time intervals; 1, 4, 8, 12, 18, 18, 22, 27, 39, 46, 53, and 60 days. The analysis of impedance spectra was done by fitting appropriate equivalent circuits using Gamry software. The coating mechanism and other phenomena were recognized by interpreting the changes of each element in the matching equivalent circuit. All the electrochemical tests were repeated at least triple to verify the reproducibility.

3. Results and discussion

3.1. Structure and morphology of MLDH and ZLDH

Different characterization tests were performed on the synthesized LDH powder to verify the adopted procedure was correct. Accordingly, the XRD patterns, FTIR spectra, and Raman analysis results of the different pristine LDH composite samples are presented in Fig. 3. Fig. 3a illustrates the XRD pattern of the prepared ZLDH and MLDH samples. Both samples display sharp and symmetric peaks associated with the

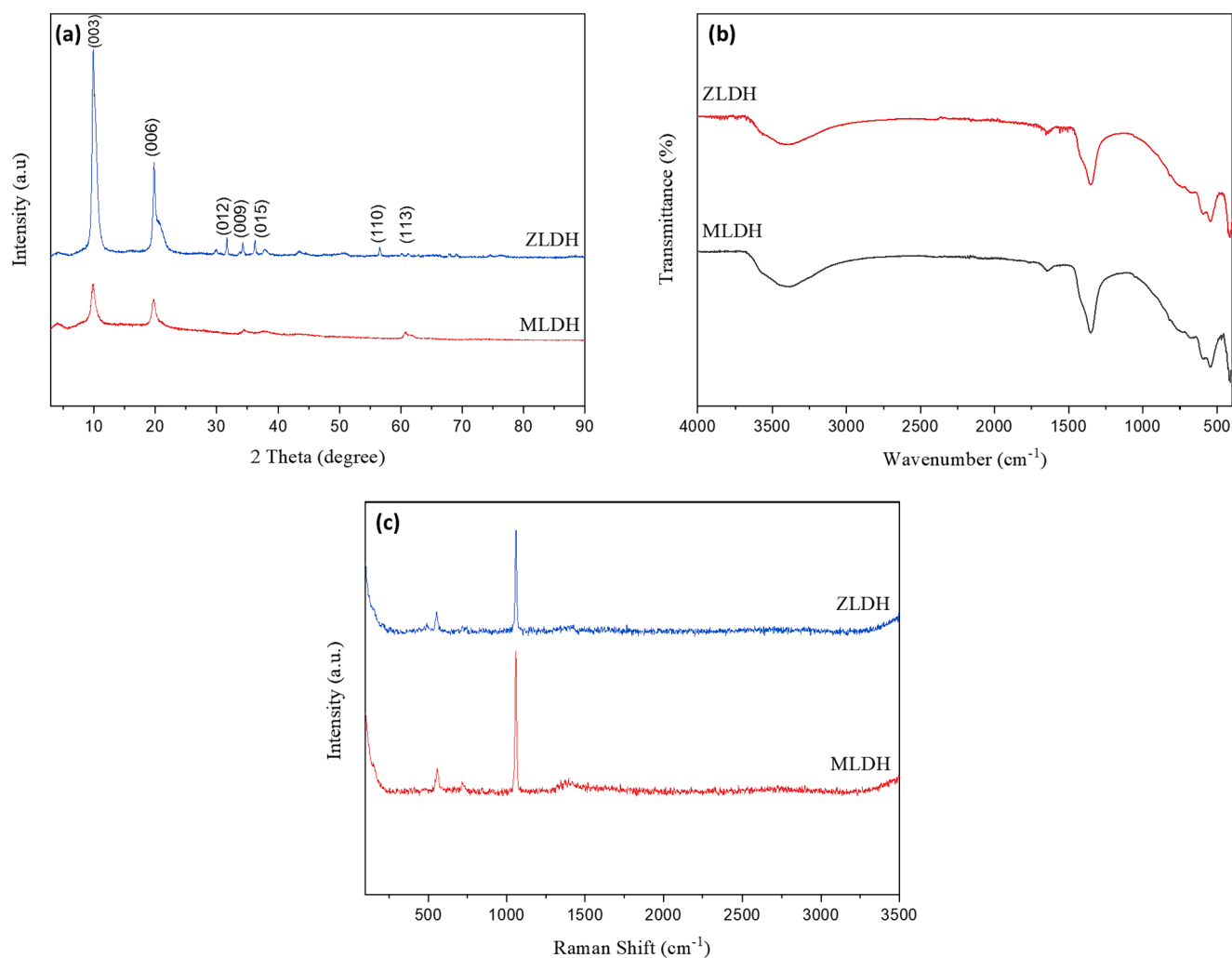


Fig. 3. (a) XRD patterns, (b) FTIR spectra, and (c) Raman spectra for the synthesized ZLDH and MLDH powder.

(003) and (006) crystal planes at lower 2θ values while (113) at higher 2θ values peaks are less intense (Basu et al., 2014). These results indicate the hydroxide nature of the materials having a high degree of crystallinity, the structure of which consists of layers of mixed divalent and trivalent metals hydroxide separated by layers of anions and water molecules (Khitous et al., 2015; A. Li et al., 2020). Diffraction on these hydroxide layers is the source of the most intense peaks in the LDH diffractograms with 2θ values between 4° and 35° (Zheludkevich et al., 2010). Other peaks corresponding to the (012), (009), and (015) planes also exist in the ZLDH sample. The appearance of (110) and (113) reflections signify the typical nature of the LDH-based materials (Muthuraman et al., 2021). Since the LDH composites were synthesized at high temperature (120°C), the crystalline and organized structure is well represented by the sharp, intense, and narrow reflection peaks (Iqbal and Fedel, 2019). Overall, the results corroborate the findings of previous studies (Gomes et al., 2020; Mikhailau et al., 2019; Yasaei et al., 2019). The features in each sample were almost identical in the FTIR spectrum. The FTIR spectra of ZLDH and MLDH (Fig. 3b) exhibit a broad adsorption band near 3420 cm^{-1} ascribed to the stretching vibration of the hydroxyl groups of hydroxide layers (Wang et al., 2018). Another absorption band at $\sim 1637\text{ cm}^{-1}$ is assigned to H-O-H bending vibration of water molecules in the interlayer spacing (Klopprogge et al., 2004; A. Li et al., 2020; Yasaei et al., 2019). The appearance of the sharp

strong peak assigned to the asymmetric stretching bond at $\sim 1350\text{ cm}^{-1}$ is attributed to the existence of NO_3^- in the LDH samples indicating successful intercalation of nitrate ions in the interlayer of LDH. (Cavani et al., 1991). Furthermore, the metal–oxygen stretching vibrations in the brucite-like layers are observed at low wavenumber range ($\sim 541\text{--}600\text{ cm}^{-1}$) (Khitous et al., 2015). Raman spectroscopy is used in conjunction with XRD results to identify LDH composites. Fig. 3c displays the Raman spectra of the pristine ZLDH and MLDH. The band near 550 cm^{-1} is associated with Zn–O–Al and Mg–O–Al. The weak band at $\sim 710\text{ cm}^{-1}$ and strong band at $\sim 1050\text{ cm}^{-1}$ regions are the characteristics of nitrate ions specifically and anions intercalated in LDH-related materials (Benício et al., 2018). These results demonstrate that the LDH composites were successfully synthesized using the combined co-precipitation and hydrothermal process.

Fig. 4 shows the surface morphology of MLDH and ZLDH obtained by scanning electron microscopy technique. Both LDH composites are clumps of LDH crystallites in their morphology. As shown in Fig. 4a and b, the MLDH exhibited a smooth surface structure aggregated with hexagonal shape flakes with varied particle sizes. The size of MgAl particles is between nano to micrometers. Beside the flake-like shape, the ZLDH particles showed rod-like shape structure with sharp edges. The thickness of ZnAl particles is in the range of 0.1 to $1\text{ }\mu\text{m}$ and length 2–5 μm .

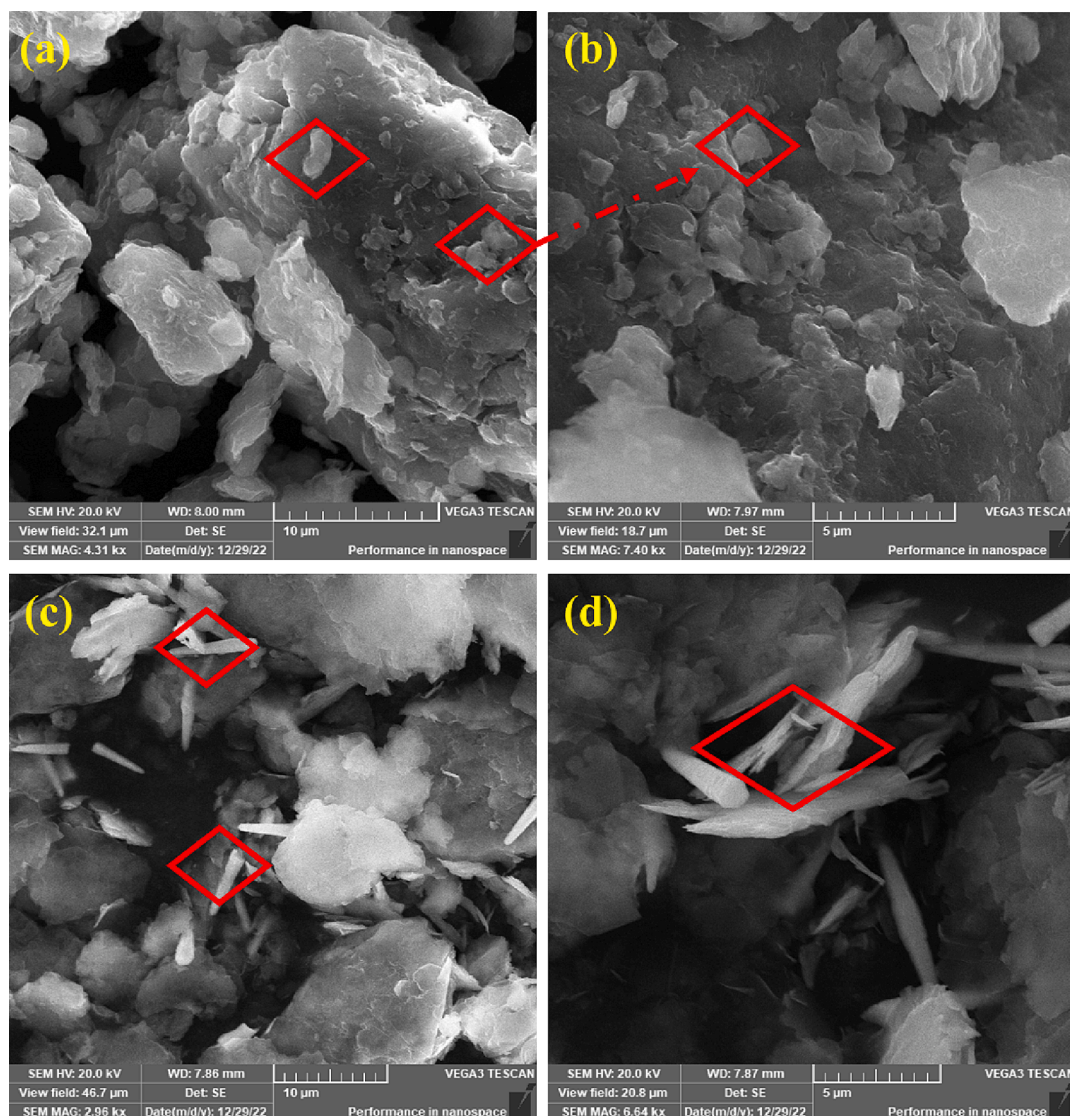


Fig. 4. SEM images of (a, b) MLDH, and (c, d) ZLDH at different magnifications.

Elemental mapping was carried out to verify that LDH samples are developed properly, and also to observe uniformity among the elements that are involved besides the atomic percentage of O, N, Al, Mg, and Zn in the synthesized LDH samples. The EDS mapping of MLDH and ZLDH is shown in Fig. 5; the uniform distribution of the elements is obvious in the samples. The successful fabrication of LDH composites is suggested by the uniformity of the components. Moreover, the experimental atomic percentage of Mg and Al was found to be 14.66 and 6.93 % for MLDH, and Zn and Al 18.27 and 7.27 % for ZLDH, respectively. These results are compatible with the molar ratio of M_{II}/M_{III} that is composed for LDH preparation.

3.2. Characterization of coated samples

The surface topography and cross-section of the bare substrate sample, neat PVDF, MLDH@PVDF, and ZLDH@PVDF are displayed in Fig. 6. A low-resolution SEM image of a top view of the bare steel substrate shows that the surface is relatively smooth (Fig. 6a and b). However, as displayed in the SEM images of neat PVDF coating (Fig. 6c and d) the surface is rugged with many bumps. The morphology of a cross-sectional area of the neat PVDF coating is shown in Fig. 6e, indicates a croissant-like shape with different pores and holes sizes. The average diameter of these holes is in the range of 2–10 μm for the prepared neat PVDF coating. Consequently, such a porous structure of the neat PVDF leads to the accessibility of the corrosive electrolyte to the metal surface and causes localized corrosion. After the addition of MLDH composite (Fig. 6f and g), the surface topography has significantly changed and become more uniform, flat, and smoother surface for all the tested steel samples. Fig. 6h and k depict the micrographs of the cross-sectional view of MLDH@PVDF and ZLDH@PVDF, respectively. The three-dimensional (3D) porous structure in both the LDH coatings disappeared and were totally filled, indicating that the small-sized LDH platelets and PVDF have been successfully bonded. Combining the above SEM observation and particle size analysis results of LDHs powder, we can deduce that the size of LDH composites is compatible with the size of holes making a homogeneous composite coating substance. Therefore, a

compact and dense coating is obtained, leading to the delayed penetration of the corrosive medium (L. X. Li et al., 2020).

In addition, the elemental composition of the coatings was investigated using EDX spectra. The EDX spectra demonstrated the existence and homogeneity of F, C, Mg, Zn, and Al in the coated samples, as shown in Fig. 7. EDX elemental maps show that the applied PVDF coatings are rich in F, and most likely C, while being Fe deficient with respect to bare steel substrate. This specifies that the as-prepared coatings were compact and fully covered the mild steel surface. As displayed in Fig. 7 (b, c, and d), the uniform distribution of F, C, Mg, Al, and Zn was observed indicating that the homogeneous matrix was obtained.

The surface roughness of bare steel substrate, neat PVDF, MLDH@PVDF, and ZLDH@PVDF coatings is shown in Fig. 8. The surface smoothness of a coating often decreases with increasing root-mean square roughness (Sq) (Lin et al., 2019). The roughness of the bare steel substrate was only 0.2817 μm which supported the above SEM analysis. The measured Sq of the coated samples was significantly increased compared with the polished bare steel sample indicating that the polymeric coatings can increase surface roughness. For instance, the three-dimensional surface roughness image of the mild steel coated by PVDF depicts a very rough and bumpy surface feature (Fig. 8b) with a surface roughness (Sq) of 14.51 μm . In contrast, the overall surface of the MLDH@PVDF sample was flat with a small surface roughness of 3.536 μm . The surface of the ZLDH@PVDF sample was a thistle-like structure and the surface showed an obvious rough appearance which makes the Sq increase to 7.76 in Fig. 8d. These observations are also consistent with SEM observation.

The surface wettability of the bare steel substrate, neat PVDF, MLDH@PVDF, and ZLDH@PVDF was evaluated using static water contact angle (WCA) measurements. The water contact angles of the fabricated PVDF coatings are presented in Fig. 9. Hydrophobicity is an essential surface property for corrosion protection since it prevents biocorrosion, icing, and fouling as well as repelling water and aqueous electrolytes. The two factors that mainly influence the degree to which a solid repels a liquid are surface energy and morphology of the surface. Hydrophobicity is known to increase with reduction in the surface

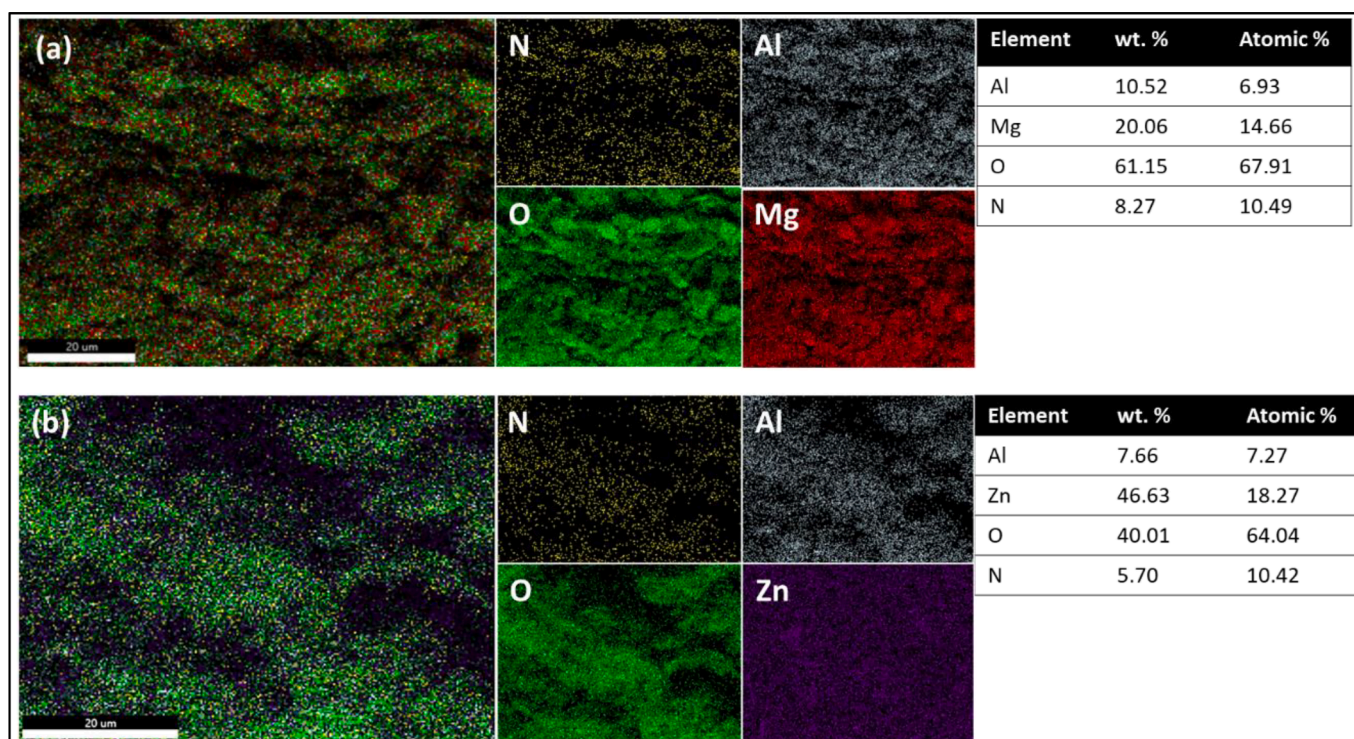


Fig. 5. The corresponding SEM-EDS map for O, N, Mg, Zn, and Al for (a) MLDH, and (b) ZLDH samples.

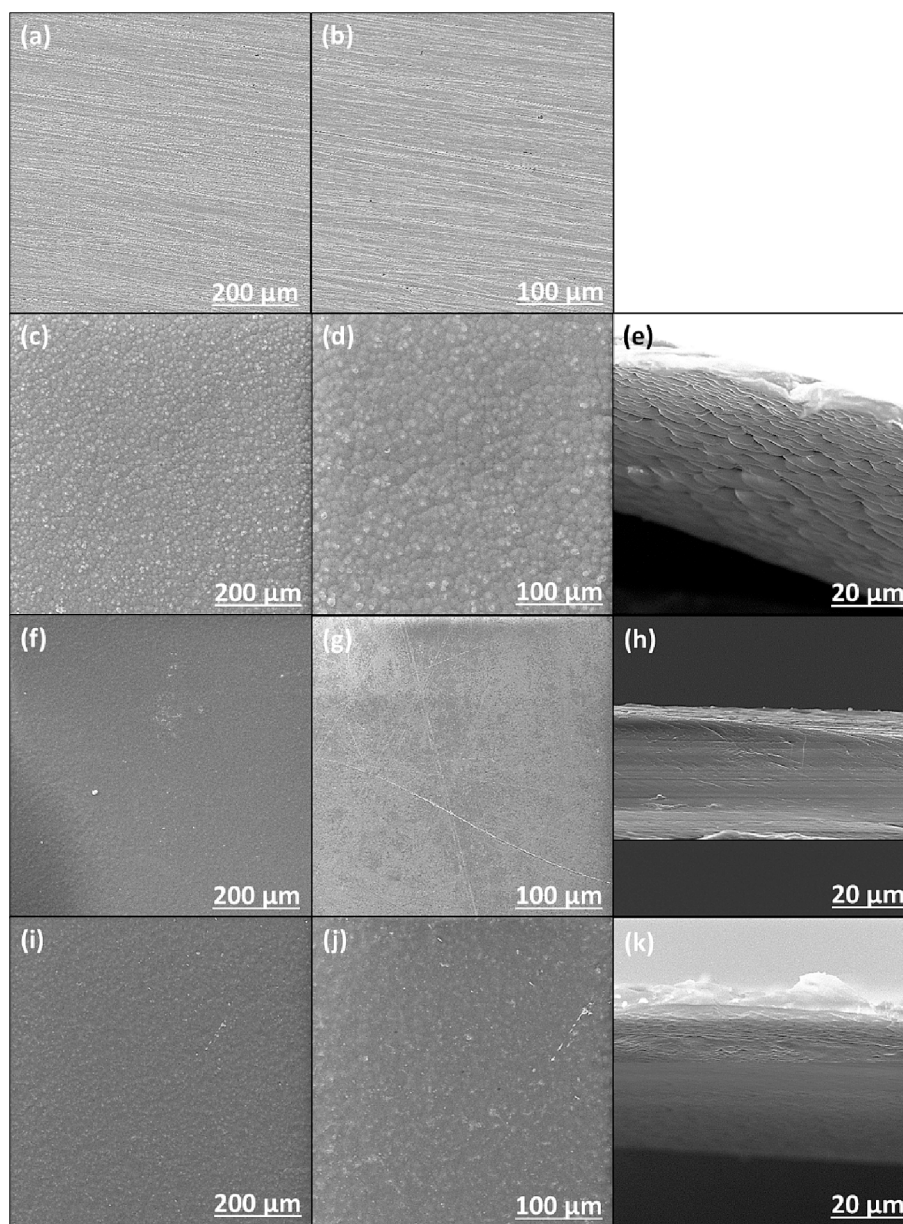


Fig. 6. SEM images of the surface and cross-section of uncoated and coated samples at different magnifications; (a, b) uncoated steel, (c, d, e) neat PVDF, (f, g, h) MLDH@PVDF, and (i, j, k) ZLDH@PVDF.

energy and increasing the micro/nano scale surface roughness. Fluorine-coated surfaces (CF_n) are widely recognized as an effective approach to generate hydrophobic or superhydrophobic coatings. The CF_n group, with its low surface energy, contributes to the hydrophobic nature of the coating (Mohamed et al., 2015; Montemor, 2014).

The obtained results confirmed the hydrophilic character of all the tested samples. As shown in Fig. 9a and b, the bare steel substrate surface changed from high hydrophilic ($WCA = 39^\circ \pm 2$) to less hydrophilic when the neat PVDF was applied, ($WCA = 80^\circ \pm 2$). This observed reduction in hydrophilicity was attributed to increase the roughness besides the lower surface energy (25 dynes cm^{-1}) due to the presence of fluorine atoms in the polymer used (Vicente et al., 2021). The pure PVDF coating has the highest contact angle of 80° compared with other coatings, indicating a relatively less hydrophilicity due to the surface structure (bump morphology), low surface energy, and a large number of pores in the coating as presented in the previous SEM and roughness images (Poss et al., n.d). Moreover, the anti-adhesion property results obtained from the adhesion tests of the coating surfaces corroborate well

with their respective large water contact angles.

Following the incorporation of LDH platelets into the composite coatings (Fig. 9c and d), the contact angle further decreases by 6.25 %. This decline is attributed to the hydrophilic nature of LDH. Notably, LDH composites possess a significant quantity of hydroxyl groups on their surface, as established earlier by XRD analyses. These hydroxyl groups enable LDH composites to adsorb a substantial amount of water molecules. It is important to note that although the contact angle of neat PVDF coating is greater than that of other coatings due to its higher roughness value, it still remains below 90° , indicating that the coating surface is not hydrophobic. This assertion is supported by SEM and roughness results.

The adhesion test (cross-cut test) is a popular qualitative technique employed to evaluate the adhesion of coatings. It entails creating a grid pattern on the coating by making multiple cuts with a blade. The quality of adhesion is assessed by visually inspecting the cut lines and identifying any signs of coating detachment or flaking (Mohammadkhani et al., 2020). The adhesion test was performed on the neat PVDF and

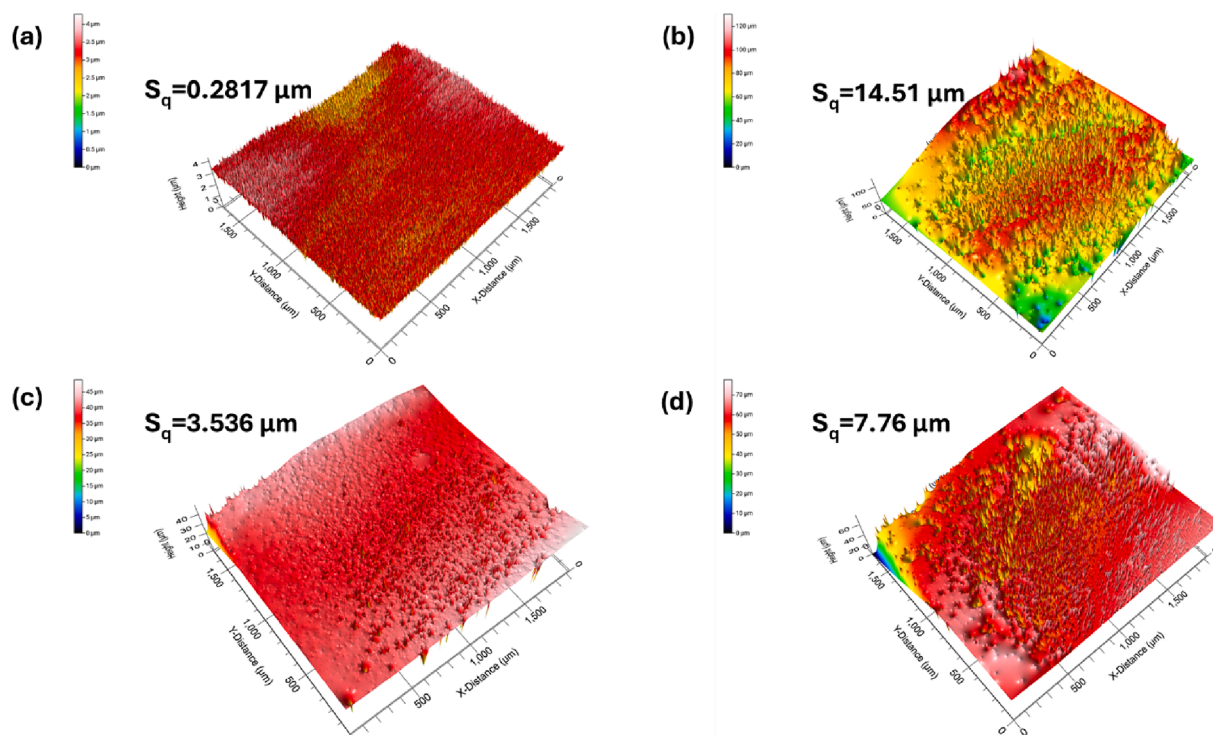


Fig. 7. 3D roughness images of the surface (a) uncoated steel, (b) neat PVDF, (c) MLDH@PVDF, and (d) ZLDH@PVDF coatings.

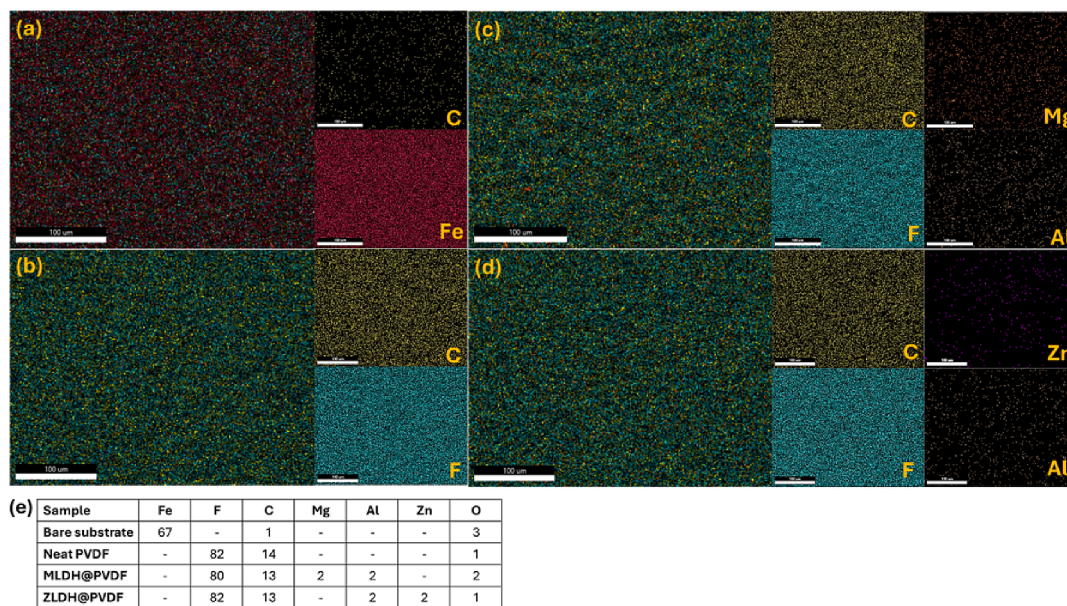


Fig. 8. EDX characterization of (a) bare steel, (b) neat PVDF, (c) MLDH@PVDF, (d) ZLDH@PVDF coatings, and (e) EDX elemental composition of uncoated and the coated mild steel samples (at. %).



Fig. 9. WCAs of (a) bare substrate, (b) neat PVDF, (c) MLDH@PVDF, (d) and ZLDH@PVDF composite coatings.

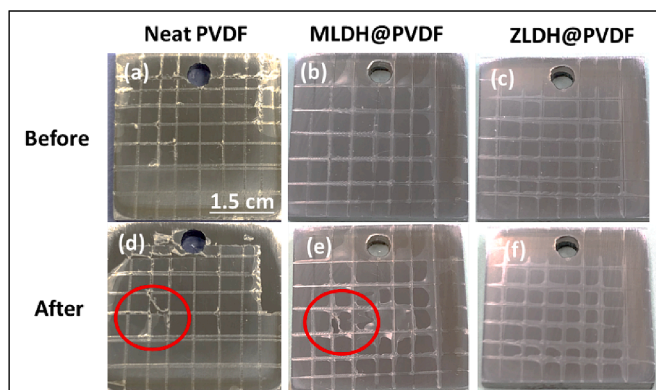


Fig. 10. Cross cut adhesion test for the composite coatings before and after the crosshatch tape; (a, b) neat PVDF, (b, e) MLDH@PVDF, and (c, f) ZLDH@PVDF.

LDH composite coatings as shown in Fig. 10. The effectiveness of the applied coatings depends on the degree of their adhesion to the substrate (Jin et al., 2020). According to the test, the neat PVDF coating (Fig. 10a and d), the adhesive failure of the coating is clearly observed with a rating of 3B. The friction of the surface can easily damage the superhydrophobic coating due to the softness of PVDF, which reduces the adhesion to most substrates thereby reducing its superhydrophobicity (Qian et al., 2021). The electrostatic force such as van der Waals forces between the steel substrate and the neat PVDF coating, is responsible for the interfacial adhesion. The diffusion of electrolytes is prone to break these weak bonds. Meanwhile, the electrochemical reactions taking place at the cathodic and anodic sites can result in the formation of hydroxyl ions and iron cations, respectively. The degradation of intermolecular or interfacial bonds, along with the subsequent separation of the coating layers would eventually, results in the diminishing of the adhesion between the coating and the substrate.

The incorporation of LDH composites into the PVDF coating is expected to cause further enhancement of adhesion forces. In this study, it is clear that the addition of LDH sheets directly improves the interfacial adhesion between PVDF and steel substrate as evidently shown in Fig. 10(b and e), the MLDH@PVDF coating's ASTM 4B rating indicates

that. According to the literature (Mohammadkhani et al., 2020), the strong adhesion of the ZLDH@PVDF coating onto iron oxides on the mild steel (MS) surface was strongly attributed to the adsorption of LDH the hydroxyl group (Fig. 10(c and f)). Therefore, ZLDH@PVDF coating exhibited the highest substrate adhesion. After the adhesion test, no detachment of any kind was observed on the surface, as shown in Fig. 10 (f), which indicates its potential for long-term protection in corrosive environment. This implies that the synthesized coating adheres well to the carbon steel substrate. The observations are strongly supported by the EIS and Tafel test results presented in the subsections below.

3.3. Formation mechanism of LDH-platelets@PVDF coating

The mechanism of formation of the composite coating is postulated to have occurred via main three main steps as presented in Fig. 11. Step I: At the beginning, the LDH composites (multiple layers) were fully exfoliated into LDH platelets (single sheets) using dimethylformamide (DMF) solvent via top-down exfoliation process. This process resulted in obtaining a milky colloidal homogeneous solution of LDH single-layered nanosheets characterized with large specific surface area. This approach ensures the utility of every single layer is maximized (Yu et al., 2017). The delamination of LDHs in DMF is thought to occur in two stages: (1) a certain volume of the DMF replaces the water molecules, resulting in a highly swollen phase, and (2) complete exfoliation is achieved through magnetic stirring. The exfoliation of the nanosheets is mainly, responsible for achieving the most desirable morphology (Honarvar Nazari et al., 2022). Step II: the PVDF particles were well-dispersed in the as-prepared homogeneous solution, thereby, forming hydrogen bonding networks between the fluorine atoms in PVDF and hydrogen atoms in the LDH hydroxyl groups (Mochane et al., 2020). Increased in electrostatic repulsion between PVDF particles improved their dispersion (Shen et al., 2021). However, the hydrophobic nature of polymers and the hydrophilic nature of LDHs make them immiscible during composite preparation (Quispe-Dominguez et al., 2019). Fortunately, the DMF plays a great role in linking PVDF and LDH. Step III: the final step involved the DMF solvent been evaporated after heating the coatings in an oven at 155C for 2 h.

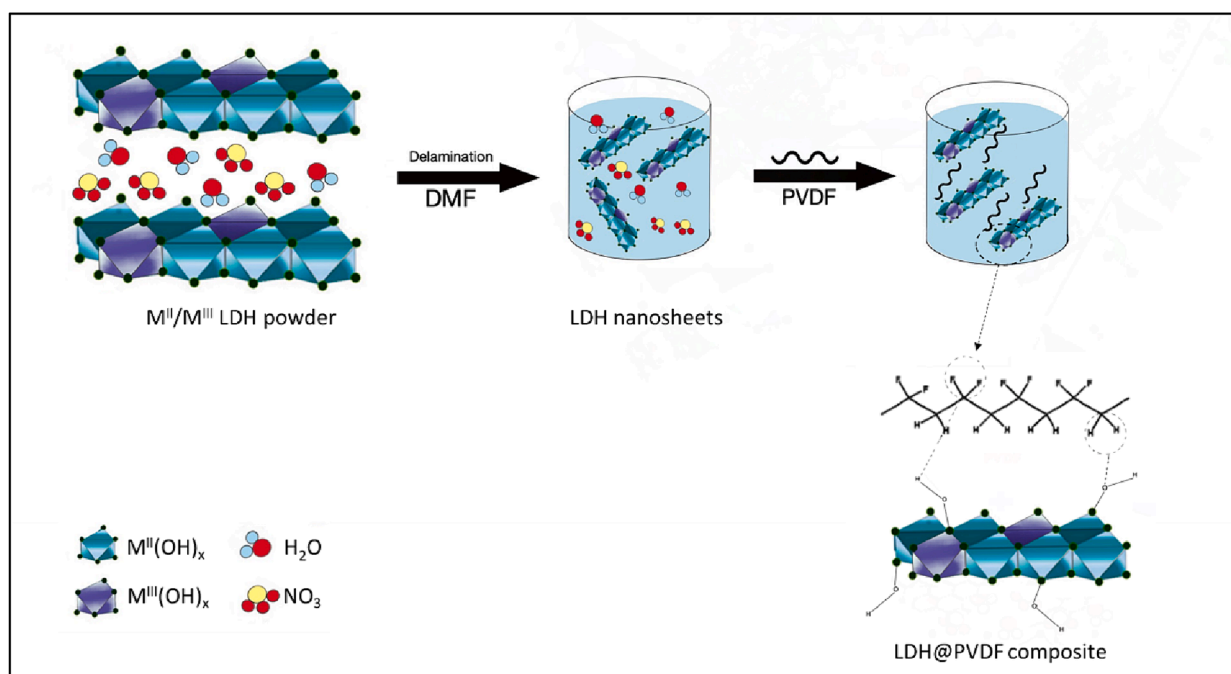


Fig. 11. The schematic diagram of LDH delamination and gel formation in DMF.

3.4. Corrosion studies

3.4.1. Open circuit potential (OCP)

Open circuit potential (E_{oc}) results of the bare steel substrate and the coated samples are presented in Fig. 12. It can be seen that the bare substrate presents the most negative OCP compared to the coated samples (-0.630 V vs. SCE) indicating the high dissolution of the mild steel sample due to increasing the cathodic reactions (oxygen reduction) when exposed to 3.5 wt% NaCl solution. Moreover, the instability attitude was observed in the neat PVDF coating evidently, from the significant decrease in the E_{oc} value down to -0.003 V, indicating higher corrosion tendency. Besides, this declining trend is attributed to the continuous water seepage through the pores and the eventual coating failure. The results clearly indicate that OCP of the LDH@PVDF composite coatings remains stable after 60 min which suggests that the system has reached a steady state. Meanwhile, the inclusion of LDH composites in PVDF coatings improved the OCP values, indicating a shift towards more noble potentials. This demonstrates that the LDH structure successfully acted as a barrier, effectively blocking corrosive media from reaching the metal surface. Relative to SHE, the potentials of the samples are recorded as -0.389 V for the bare substrate, 0.244 V for neat PVDF, 0.274 V for MLDH@PVDF, and 0.293 V for ZLDH@PVDF, respectively. At this approximate pH of the solution (6.8), and as per the Pourbaix diagram, the potential range falls within the active corrosion area. Particularly, the ZLDH@PVDF coating demonstrates the most noble potential among all tested coatings.

3.4.2. Potentiodynamic polarization measurements (PDP)

Fig. 13 shows that PDP measurements were taken to determine the corrosion resistance of mild steel samples in 3.5 % NaCl medium both without and with the investigated coatings (i.e., neat PVDF, MLDH@PVDF, and ZLDH@PVDF). Prior to the potential sweep, the samples were left under an open circuit for 1 h in the respective solution until a steady state corrosion potential was reached. The corrosion behavior of the coated steel is evaluated by comparing the polarization curve of the coated sample with that of the bare steel. Parameters such as corrosion potential (E_{corr}), corrosion current (i_{corr}), Tafel slopes (β_a and β_c) and polarization resistance (R_p) can be derived from the polarization curve. These parameters provide insights into the corrosion rate, corrosion protection efficiency, and performance of the coating in inhibiting the corrosion process. The polarization resistance (R_p) is calculated using the Stern–Geary equation (Han et al., 2021):

$$R_p = \frac{\beta_a \beta_c}{2.303(\beta_a - \beta_c) i_{corr}} \quad (1)$$

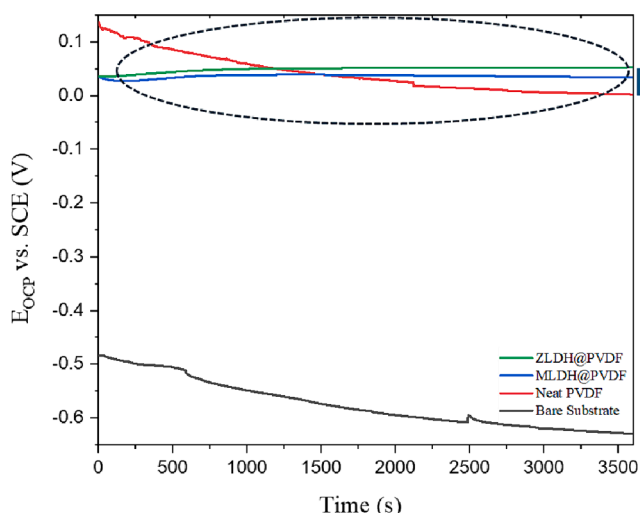


Fig. 12. Open-circuit potential behavior of the bare mild steel substrate and LDH PVDF composite coatings.

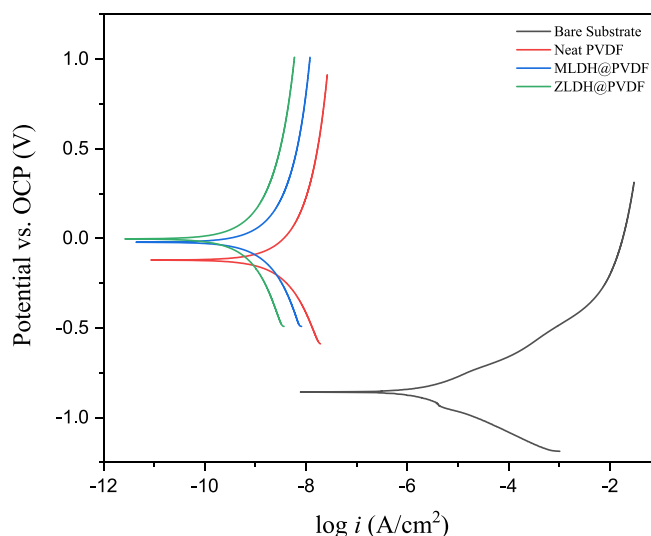


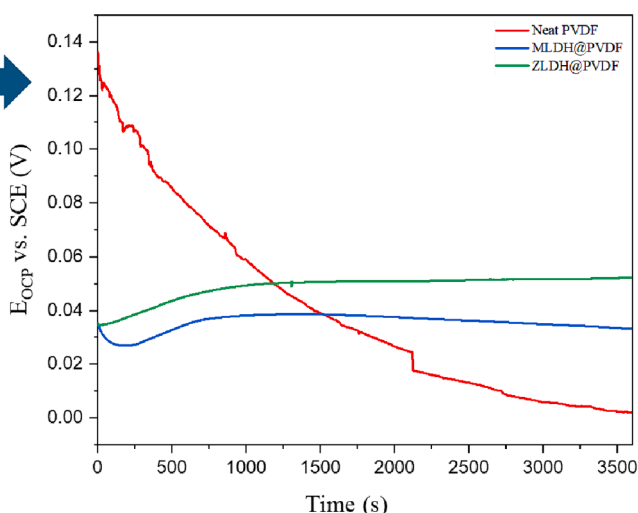
Fig. 13. PDP curves for the bare substrate and those coated with neat PVDF, MLDH@PVDF, and ZLDH@PVDF in a 3.5% NaCl solution.

Table 2

Tafel fitting results from the potentiodynamic polarization curves.

Specimens	E_{corr} (mV vs. OCP)	i_{corr} ($\mu\text{A}/\text{cm}^2$)	Tafel slope β_a (mV/dec)	β_c (mV/dec)	R_p ($\Omega\cdot\text{cm}^2$)
Bare substrate	-857	1.85	0.138	0.132	7.91×10^{-1}
Neat PVDF	-123	1.24×10^{-2}	2.523	1.487	1.27×10^2
MLDH@PVDF	-21	6.53×10^{-3}	2.744	1.843	3.73×10^2
ZLDH@PVDF	2	2.21×10^{-3}	1.795	1.595	2.81×10^3

Where β_a and β_c are anodic slope and cathodic slope, respectively. The results clearly demonstrate that the i_{corr} values of the coated samples were significantly lower than those of the bare steel substrate (Table 2). In general, a lower i_{corr} indicates superior corrosion resistance and vice versa. Applying PVDF alone on the bare steel samples resulted in a significant decrease in the corrosion current density (i_{corr}) from $1.85 \mu\text{A}/\text{cm}^2$ (for the bare substrate) to $1.24 \times 10^{-2} \mu\text{A}/\text{cm}^2$. Moreover, the corrosion potentials, E_{corr} , of the LDH composite coatings shifted noticeably toward a more noble or passive direction compared to the bare substrate. This shift indicates a delayed initiation of the corrosion



process, indicating a robust protective mechanism. Some previous studies had reported that the corrosion potential of anticorrosion coatings generally nudges the corrosion potential towards positive values (Zhang et al., 2014). However, the E_{corr} alone is not sufficient to evaluate the anti-corrosion performance of the coatings, as it primarily indicates the thermodynamic behavior of the materials (Chen et al., 2021), as such the corrosion data are supported by the Tafel measurements.

Tafel constants for anodic (β_a) and cathodic (β_c) reactions provide an evaluation of the reaction kinetics, with higher values indicating slower reactions, implying that higher values are generally better for corrosion resistance. Accordingly, the steel coated samples with MLDH@PVDF and ZLDH@PVDF show higher β_a and β_c values, suggesting an improved corrosion resistance compared to both the bare substrate and neat PVDF-coated sample.

The data presented in Table 2 compares the corrosion potential of the bare substrate and ZLDH@PVDF coating. The ZLDH@PVDF coating led to significant improvement of the steel samples corrosion protection as the corrosion potential decreased from -857 mV to 2 mV vs SCE. Additionally, the corrosion current decreased from $1.85 \mu\text{A}/\text{cm}^2$ to $2.21 \times 10^{-3} \mu\text{A}/\text{cm}^2$, and the polarization resistance climbed by four orders of magnitude (from $7.91 \times 10^{-1} \Omega/\text{cm}^2$ to $2.81 \times 10^3 \Omega/\text{cm}^2$). This significant improvement was attributed to the effective blocking of pores and microdefects by the modified LDH sheets in the coating, thus hindering the corrosion medium's diffusion. The inclusion of LDH composites improves the corrosion resistance of the coatings, thereby providing excellent protection.

The primary factors that lead to the dissolution of mild steel is the presence of chloride ions, O_2 , and H_2O within the vicinity of the steel surface, which promotes anodic oxidation and cathodic reduction (oxygen reduction) reactions to take place, and thus subsequent formation

of corrosion. By impeding the diffusion of these species to the surface of mild steel, an effective barrier coating such as LDHs@PVDF results in a significant reduction in the corrosion current, providing substantial protection against corrosion (Ali et al., 2021). The PDP results (Table 2) obtained reveal that the ZLDH@PVDF coating displayed the most favorable corrosion resistance, as evidenced by its lowest corrosion current value ($2.21 \times 10^{-3} \mu\text{A}$) and highest efficiency (99.88 %). The corrosion protection efficiency of the ZLDH@PVDF coating was calculated from Tafel polarization curves using the following Eq (2) (Gu et al., 2016):

$$P_{EF}\% = \frac{i_{\text{corr}}(\text{uncoated}) - i_{\text{corr}}(\text{coated})}{i_{\text{corr}}(\text{uncoated})} \times 100\% \quad (2)$$

Hence, it can be concluded that the ZLDH@PVDF coating demonstrated superior performance in inhibiting the steel corrosion.

3.4.3. EIS studies

Electrochemical Impedance Spectroscopy (EIS) has become a recognized technique for long-term corrosion measurement. By measuring the electrical impedance at different frequencies, the corrosion behavior of a metal can be monitored and quantified. Moreover, fitting the EIS data to equivalent circuit models can provide quantitative information about different corrosion processes. There are generally two major components contributing to the EIS in corrosion studies: the charge transfer resistance (associated with the electron transfer between a metal been tested and an electrolyte) and the mass transport impedance (related to the diffusion of ions in the electrolyte which is denoted as Warburg component). Fig. 14 depicts the Nyquist plots for all of the coated steel samples (compared to the bare steel sample) under 60 days

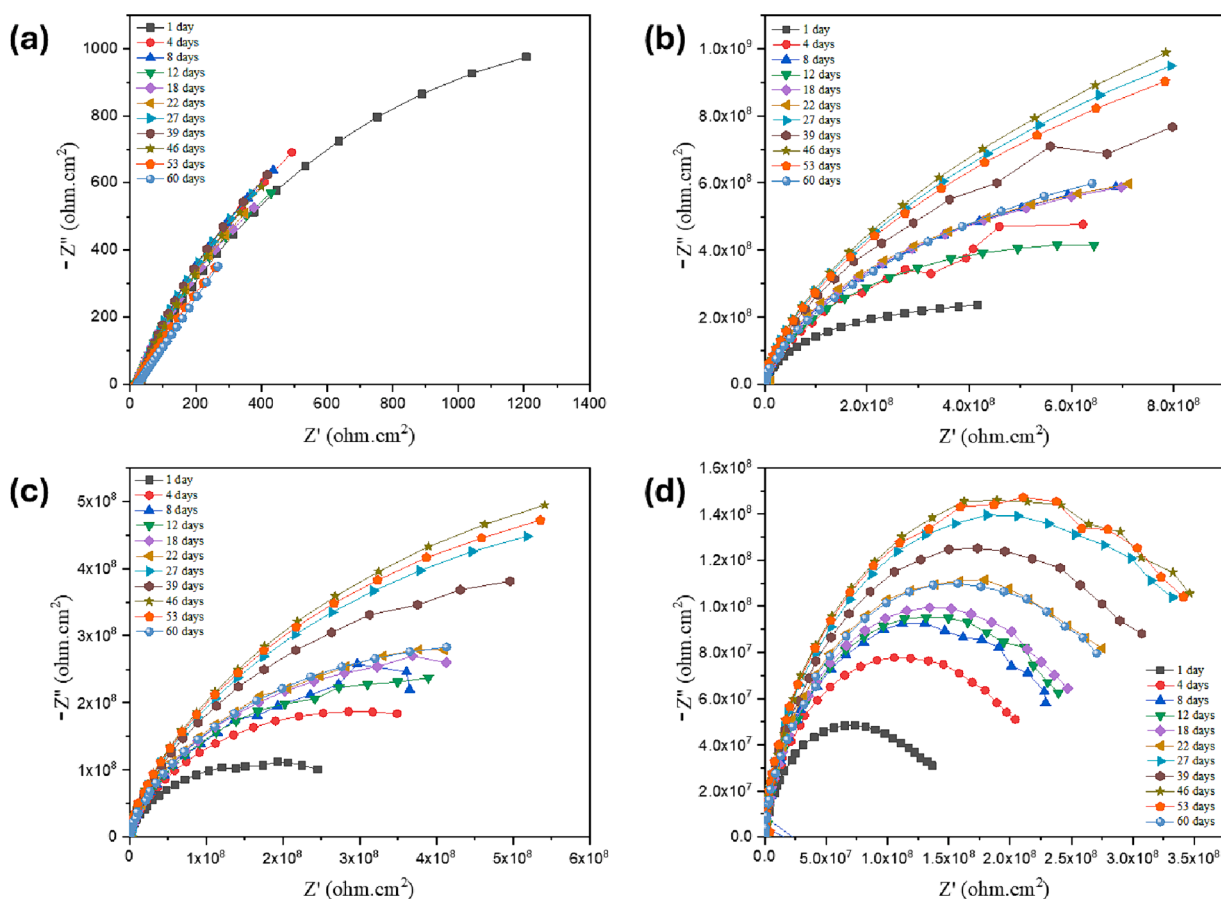


Fig. 14. Nyquist Plots from long-term measurements for (a) Bare steel sample (b) Neat PVDF coated (c) MLDH@PVDF coated and (d) ZLDH@PVDF coated steel samples in 3.5% NaCl solutions.

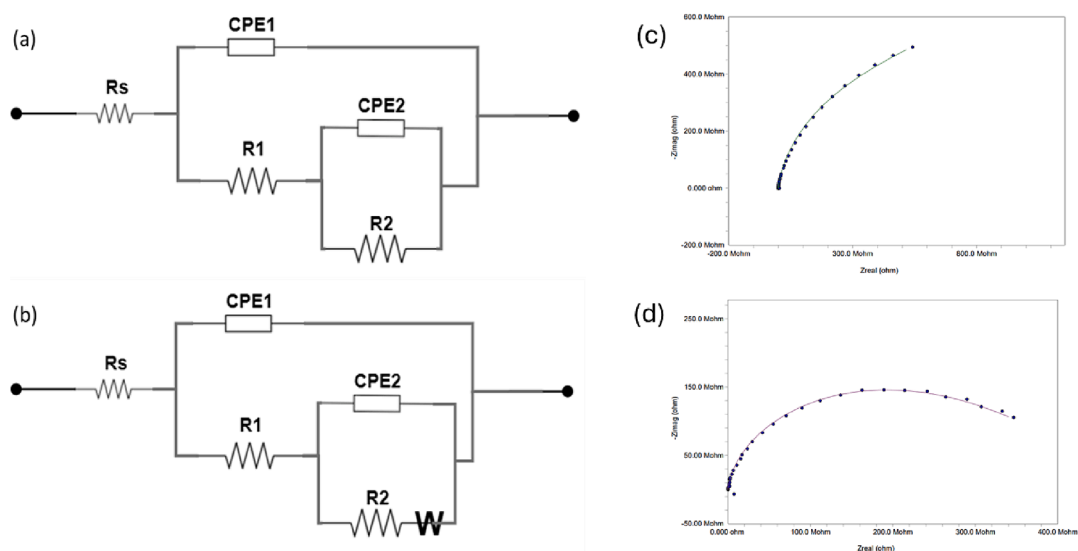


Fig. 15. Equivalent circuits from fitting the EIS spectra (a) bare steel from 1 h to 60 days, MLDH@PVDF (1 h and 1 day), Neat PVDF (1 h), and ZLDH@PVDF from 1 h to 60 days, (b) MLDH@PVDF (4 days to 60 days) and Neat PVDF (1 day to 60 days), (c) fitting of MLDH@PVDF coating after 46 days of immersion, and (d) fitting of ZLDH@PVDF coating after 46 days of immersion.

long-term EIS measurements in 3.5 % wt. NaCl solutions. Meanwhile, Fig. 15 displays the corresponding equivalent circuits (EC) model of the electrochemical system at the interfaces for each of the samples and an example of fitting for ZLDH@PVDF sample. The corresponding Bode plots are shown in Fig. S1. Generally, all the samples were found to perfectly fit the equivalent circuit with two constant phase elements (CPEs), thereby exemplifying the two different interfaces of the coated samples i.e., electrolyte/coating (CPE1) and coating/substrate (CPE2). The data extracted from the EIS spectra fitting are tabulated in Table 3, where R_s represents the ohmic solution resistance, CPE represents, R_1 and R_2 denote the resistance of the electrochemical charge transfer process at the two interfaces. While the EIS measurements for all samples generally exhibit a consistent trend of increase or decrease, occasional irregularities are observed. It's important to note that each reported value represents an average of at least three replicates, ensuring data reliability and accuracy. The impedance of a CPE is given by the following equation:

$$Z = \frac{1}{Y(j\omega)^n} \quad (3)$$

In this context, Z represents impedance and Y denotes admittance, quantifying the system's electric charge traversal ease. In an ideal system, admittance is the reciprocal of impedance. 'j' is the imaginary unit, ' ω ' stands for angular frequency, and 'n' represents the exponent for the constant phase element (CPE). CPE power factors signify deviation from ideal capacitive behavior: a value of 1 denotes an ideal capacitor, while a decrease from unity (a_1 and a_2) suggests increasing deviation, potentially due to increased roughness or interface heterogeneity (Isakhani-Zakaria et al., 2019). The Warburg element, being in series with the inner CPE, represents a diffusion process occurring at or near the coating/substrate interface (Fig. 15 (b)).

In addition, Fig. 16 exhibits digital photographs taken at different intervals during the long-term immersion test aiming to record and monitor any evolving developments throughout the test duration.

For the uncoated sample i.e., the bare steel, the two CPEs represent the metal oxide/solution interface and the oxide/substrate interface in the EC(a) (Fig. 15). Therefore, the decrease in the R_1 value suggests a decrease in the resistance to charge transfer due to the harsh environment and attack by chloride ions on the oxide film. On the other hand, the increase in the R_2 value indicates the formation of a corrosion product or passive layer on the steel surface which is noticeable in the

brownish color of rust starting at day 1 (Fig. 16-Bare substrate).

The EIS spectra of the neat PVDF-coated steel samples fit the EC (a) in Fig. 15 at the beginning but after 24 h, the Warburg element emerged in EC(b) until the end of the long-term test. In essence, the diffusion processes can be detected at lower frequencies of the Nyquist and Bode diagrams. This confirms the effect of diffusion of corrosive species such as chloride ions into the pores of the neat PVDF coating after a specific time of contact with 3.5 %NaCl and affects the double layer capacitance. However, the PVDF has good protection of the carbon steel samples increasing the charge transfer resistance for example from 2.1 and 1.41 k Ω for the bare steel to 160 and 330 k Ω for neat PVDF-coated steel in 1 h and 24 h tests respectively.

The EIS measurements for the MLDH@PVDF-coated samples initially conform to equivalent circuit EC(a) for the first 24 h, after which the EIS spectra align with EC(b), indicating the presence of diffusion-controlled reactions at the coating/substrate interface Fig. 14(b) and Table 3. This diffusion of corrosive species, such as chloride ions, is visually evident in digital photographs of both Neat-PVDF and MLDH@PVDF coatings, which display noticeable pitting and the presence of a dark layer beneath the coatings (Fig. 16, day 12- day 60). Notably, the inclusion of MLDH within the PVDF matrix significantly enhances the coating's corrosion protection.

In contrast, the ZLDH@PVDF-coated sample maintains consistent EIS spectra over the entire duration of the long-term testing period, spanning from 1 h to 60 days, without manifesting any diffusion element, as depicted in Fig. 14(d). This explicitly underscores the exceptional corrosion resistance exhibited by the ZLDH@PVDF coating. This assertion finds additional support in the persistent high values of resistance and low values of constant phase element (CPE) admittances. Additionally, the high and consistently stable resistance values associated with the CPEs in the ZLDH@PVDF samples underscore the presence of a robust and efficient barrier against the corrosive environment. To illustrate from EIS parameter for ZLDH@PVDF coating in Table 3, both R_1 and R_2 increased one order of magnitude by day 60.

The absence of the Warburg element in the EIS dataset for the ZLDH@PVDF coating further substantiates its efficacy as a highly proficient protective layer, effectively mitigating diffusion-controlled processes. Digital photographs taken throughout the extended experimentation period reveal an unchanging, lustrous surface for the ZLDH@PVDF coating, underscoring its robustness over the entire 60-day duration (Fig. 16).

Table 3

EIS measurements parameters for long-term immersion in 3.5% NaCl at RT.

sample	Immersion time	$R_s, \Omega \cdot \text{cm}^2$	CPE1		$R_1, \Omega \cdot \text{cm}^2$		CPE2		$R_2, \Omega \cdot \text{cm}^2$	$Z_w, \Omega \cdot \text{cm}^2 \cdot \text{s}^{0.5}$
			Y_1	a_1	Y_2	a_2				
bare substrate	1 h	31.78	4.26E-04	8.01E-01	4.14E + 02	3.74E-04	7.28E-01	2.13E + 03	–	
	1d	25.47	5.65E-04	7.62E-01	1.79E + 03	5.19E-04	6.45E-01	1.41E + 03	–	
	4d	18.25	4.83E-04	7.97E-01	16.02	1.05E-03	7.23E-01	3.97E + 03	–	
	8d	16.27	1.32E-03	6.90E-01	28.08	4.28E-04	9.12E-01	4.36E + 03	–	
	12d	16.9	2.30E-04	8.86E-01	9.574	1.53E-03	7.69E-01	2.35E + 03	–	
	18d	15.27	1.23E-03	6.86E-01	19.27	7.60E-04	8.78E-01	2.69E + 03	–	
	22d	18.29	1.38E-03	6.70E-01	18.42	7.67E-04	8.87E-01	3.32E + 03	–	
	27d	20.31	1.17E-03	6.92E-01	18.42	8.02E-04	8.88E-01	3.41E + 03	–	
	39d	22.88	1.15E-03	7.08E-01	21.86	6.17E-04	8.99E-01	3.43E + 03	–	
	46d	24.87	1.41E-03	6.98E-01	26.69	4.63E-04	9.02E-01	3.89E + 03	–	
	53d	18.16	2.87E-03	6.31E-01	27.91	2.38E-04	9.54E-01	6.12E + 03	–	
	60d	21.29	3.44E-04	8.61E-01	7.997	2.84E-03	5.92E-01	2.89E + 05	–	
	Neat PVDF	1 h	19	7.38E-10	9.55E-01	2.50E + 07	7.79E-09	3.70E-01	1.60E + 08	–
		1d	23	5.51E-10	9.79E-01	9.07E + 07	1.47E-09	5.67E-01	3.30E + 08	6.95E-09
		4d	32	5.65E-10	9.76E-01	1.30E + 07	1.76E-14	5.28E-01	2.11E + 08	1.71E-09
8d		5	6.39E-10	9.68E-01	5.00E + 08	1.37E-07	8.69E-01	1.59E + 03	1.79E-09	
12d		28	6.26E-10	9.68E-01	4.51E + 08	1.69E-09	8.71E-01	4.57E + 08	1.23E-08	
18d		19	4.51E-10	9.96E-01	3.25E + 04	6.32E-10	6.92E-01	6.05E + 08	2.27E-09	
22d		15	6.02E-10	9.70E-01	5.13E + 08	6.80E-08	1.00E + 00	5.56E + 06	1.77E-09	
27d		39	6.20E-10	9.70E-01	6.57E + 08	1.63E-08	9.57E-01	1.14E + 05	1.10E-09	
39d		33	5.97E-10	9.72E-01	5.81E + 08	7.88E-08	8.88E-01	1.02E + 05	1.29E-09	
46d		17	5.42E-10	9.91E-01	4.21E + 08	9.80E-08	9.94E-01	7.80E + 04	8.73E-10	
53d		23	6.08E-10	9.71E-01	6.55E + 08	4.23E-09	8.84E-01	2.57E + 03	1.11E-09	
60d		31	6.83E-10	9.65E-01	4.07E + 08	8.38E-09	8.86E-01	2.09E + 03	1.59E-09	
MLDH@PVDF		1 h	16	9.02E-10	9.54E-01	7.10E + 06	1.00E-08	3.08E-01	1.55E + 08	–
		1d	19	6.26E-11	9.86E-01	1.32E + 07	2.00E-09	4.98E-01	3.99E + 08	–
		4d	22	5.97E-10	9.88E-01	3.89E + 03	1.35E-09	5.42E-01	5.66E + 08	3.95E-08
	8d	32	6.39E-10	9.68E-01	5.00E + 08	9.68E-10	9.51E-01	1.59E + 03	1.79E-09	
	12d	19	7.05E-10	9.74E-01	4.20E + 07	1.31E-09	5.49E-01	5.49E + 08	1.64E-08	
	18d	17	6.79E-10	9.79E-01	4.00E + 07	1.23E-09	5.95E-01	3.00E + 08	4.70E-09	
	22d	18	8.93E-10	9.50E-01	2.00E + 03	3.42E-17	9.76E-01	3.91E + 08	5.19E-09	
	27d	17	8.14E-10	9.61E-01	3.92E + 08	8.21E-09	9.50E-01	3.55E + 04	2.17E-09	
	39d	18	5.23E-10	1.00E + 00	3.69E + 08	1.20E-09	6.74E-01	6.48E + 04	3.13E-09	
	46d	24	7.82E-10	9.62E-01	3.19E + 08	5.37E-09	9.56E-01	1.35E + 04	1.86E-09	
	53d	18	6.79E-10	9.76E-01	9.86E + 07	1.21E-09	5.84E-01	7.14E + 08	4.08E-09	
	60d	25	8.81E-10	9.54E-01	3.59E + 02	1.01E-09	3.79E-01	6.88E + 08	1.01E-08	
	ZLDH@PVDF	1 h	23	8.33E-10	9.51E-01	6.51E + 05	1.54E-08	2.80E-01	7.97E + 07	–
		1d	20	7.21E-10	9.51E-01	2.50E + 07	3.58E-09	3.65E-01	1.71E + 08	–
		4d	33	5.59E-10	9.80E-01	1.10E + 07	1.81E-09	4.00E-01	2.81E + 08	–
8d		17	7.95E-10	9.51E-01	1.56E + 08	5.58E-09	6.71E-01	1.30E + 08	–	
12d		31	5.91E-10	9.70E-01	1.15E + 07	1.50E-09	3.91E-01	3.30E + 08	–	
18d		27	6.29E-10	9.63E-01	1.29E + 07	1.43E-09	3.90E-01	3.35E + 08	–	
22d		22	4.96E-10	9.74E-01	1.42E + 07	1.14E-09	5.51E-01	3.43E + 08	–	
27d		32	6.46E-10	9.60E-01	1.48E + 08	2.47E-09	4.81E-01	3.50E + 08	–	
39d		28	6.89E-10	9.60E-01	1.03E + 08	2.44E-09	3.77E-01	3.90E + 08	–	
46d		31	5.82E-10	9.67E-01	8.44E + 06	9.77E-10	3.94E-01	4.88E + 08	–	
53d		19	5.91E-10	9.66E-01	9.28E + 06	9.77E-10	4.11E-01	4.75E + 08	–	
60d		33	7.45E-10	9.10E-01	4.50E + 06	1.04E-09	4.30E-01	3.67E + 08	–	

Collectively, these results suggest that the ZLDH@PVDF protective layer exhibited exceptional uniformity, strength, and stability, offering an explanation for the surface's enduring integrity even after prolonged exposure to a 3.5 % NaCl solution over the two-month testing period. These findings from the long-term EIS measurements align with those obtained from potentiodynamic polarization (PDP) measurements, further consolidating the robust corrosion-resistant properties of the ZLDH@PVDF coating.

3.4.4. EIS analysis of coating scratch

Another alternative method to assess the durability of LDH composite coatings in corrosive environments involves immersing coated samples after introducing an artificial scratch. Thus, to further establish the robustness of the steel coatings presented in this study, EIS analysis of scratched samples was undertaken, and the results are presented in Fig. 17. In this test, each of the coated samples (the neat PVDF, MLDH@PVDF, and ZLDH@PVDF coatings) was uniformly scratched (as shown in Fig. 17a-c, respectively) prior to immersion in the 3.5 % wt. NaCl solution for a period of 20 h. Afterwards, the changes were observed in the cut regions which are illustrated in Fig. 17d-f,

respectively. Notably, the neat PVDF coating displayed no self-healing film at the cut site (Fig. 17d), accompanied by increased signs of corrosion around the scratch. This indicates that an adhesion failure occurred due to the penetration of NaCl solution to the mild steel surface, stemming from inadequate bonding between the metal and the coating. In contrast, both MLDH@PVDF and ZLDH@PVDF coatings exhibited denser structures forming better protective films within the cut regions (Fig. 17e, f) compared to the neat PVDF coating. Meanwhile, the ZLDH@PVDF demonstrated a more resilient protective effectiveness against corrosion of the steel surpassing the performance of the MLDH@PVDF coating, corroborating the earlier presented results from the unscratched PDP and EIS measurements.

Additionally, EIS measurements were undertaken for the 20-day long-term immersion of the scratched coatings in the tested corrosive environments for the estimation of corrosion resistance. The analysis of the Nyquist diagram, presented in Fig. 18, revealed a reduction in the semicircle diameter for the neat PVDF coating, indicating a loss of corrosion protection in the presence of a superficial defect or scratch on the mild steel surface, without the addition of LDH sheets before immersion. Generally, improved corrosion resistance is associated with

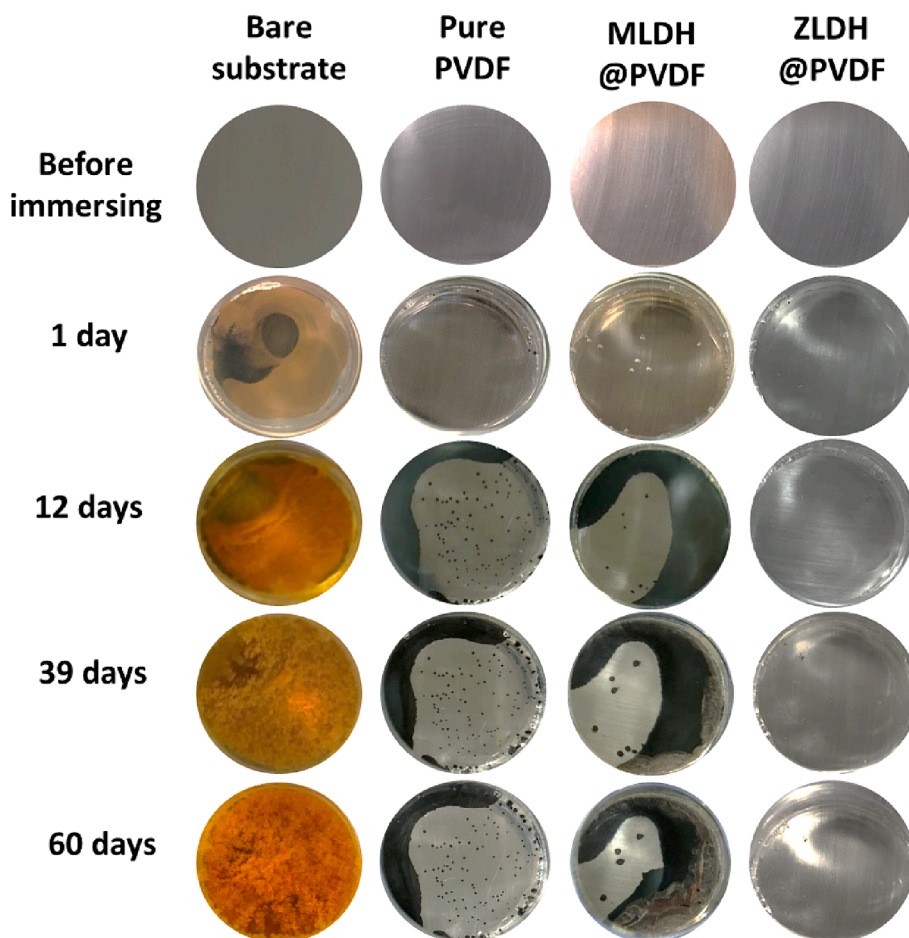


Fig. 16. Digital photographs of uncoated and coated samples up to 60 days.

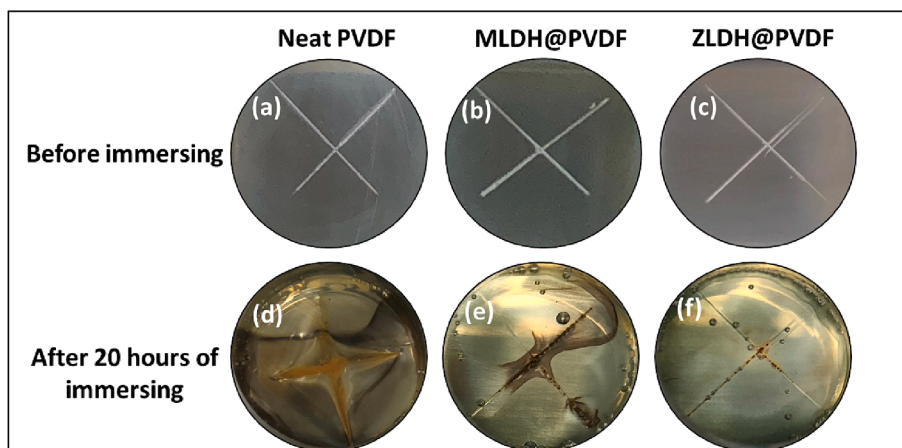


Fig. 17. Digital photographs of the PVDF composite coatings on mild steel substrate (a, b, c) before and (d, e, f) after immersion in 3.5% wt. NaCl solution for scratch test.

higher impedance modulus at lower frequencies. Conversely, the Nyquist diagram of both the investigated LDH composite coatings exhibited an increase in the semicircle diameter, with the ZLDH@PVDF coating demonstrating a significantly higher modulus than other coatings at low frequencies (Fig. 18). Notably, transition metal-based LDHs, such as zinc (ZnAl-LDH), exhibit slow ion diffusion and poor electrical conductivity, contributing to their self-healing properties and strong adhesion (Sarigamala et al., 2019; Tedim et al., 2010). The term “self-healing” refers to a material’s ability to restore its original properties

following damage from external agents or internal stresses. LDH systems exhibit three types of self-healing effects: LDH recrystallization, cation release, and inhibitor release from the LDH framework. In the absence of an inhibitor, the dissolution/recrystallization of LDH and cation release are the most likely mechanisms. In the presence of an artificial scratch, the ZnAl-LDH crystal may be destroyed, releasing Zn^{2+} and Al^{3+} cations that can recrystallize within the scratch, forming a new ZnAl-LDH crystal. This inherent characteristic of ZnAl-LDH contributes to its self-repair and, consequently, enhances the steel’s corrosion resistance.

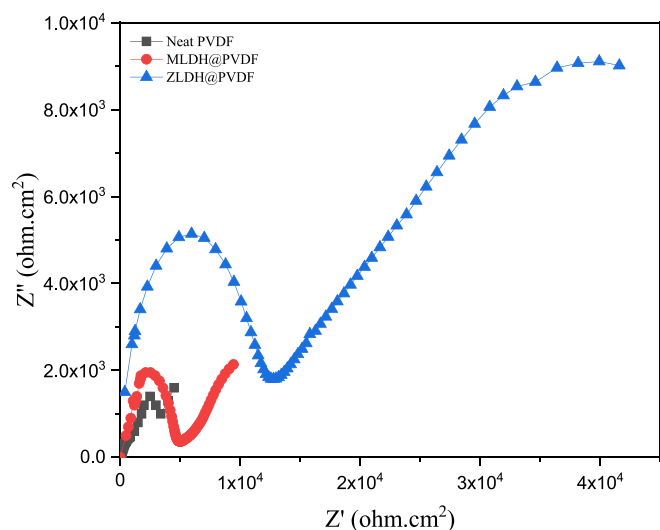


Fig. 18. Nyquist plot for the scratched PVDF composite coatings after 20 days of immersion in 3.5 % wt. NaCl solution.

Furthermore, the partial dissolution of Zn^{2+} and Al^{3+} cations from LDH positively affects corrosion inhibition by promoting the formation of zinc, aluminum oxide, or hydroxide films on mild steel when LDH is immersed in alkaline solutions (Cao et al., 2022).

3.5. Mechanism of corrosion protection of ZLDH@PVDF coating

The experimental results presented in the previous section demonstrated that the ZLDH@PVDF coating shows adequate inhibition and robustness in preventing corrosion of the steel substrates compared to both the MLDH@PVDF and neat PVDF coatings. The proposed inhibitory mechanisms of the ZLDH@PVDF are depicted in Fig. 19. The significant improvement in corrosion inhibition of the ZLDH@PVDF coating can be deduced to be as results of several factors and mechanisms that occurred as follows:

1. Barrier Protection and Labyrinth Effect: The LDH sheets dispersed in the coating matrix acted as fillers in defects, micropores, and/or nanopores, increasing the tortuosity and hindering the permeation of water and gas molecules. This labyrinth effect creates a more tortuous transport/diffusion path, preventing corrosive substances from reaching the substrate surface. As displayed in Fig. 19, the coating structure on the steel surface provides a passivating layer, that acts as a barrier inhibiting the diffusion of oxygen, chloride ions, and water molecules due to the LDH sheet structure.
2. Surface Roughness: the nature of the roughness of ZLDH@PVDF coating could lead to decrease the corrosion tendency ...
3. Enhanced Adhesion and Interactions: The incorporation of ZLDH in the coating assembly with PVDF improves the adhesion and anti-corrosion properties (Tedim et al., 2012). The increased interactions between the ZLDH composite coating and mild steel enhance the overall effectiveness of the coating in preventing corrosion.
4. Zinc Presence and Crystallite Size: The presence of zinc in the LDH array contributes to better corrosion protection (Gomes et al., 2020). The larger crystallite size of ZLDH, determined through X-ray diffraction analysis, is more suitable for the porous size, enhancing the protective properties of the coating (Table S1). Additionally, the crystallite size affects the bridging between polymer molecules, leading to a higher crosslinking thickness of the restored polymer.

Overall, the mechanisms involved in the superior corrosion resistance of the ZLDH@PVDF coating on the mild steel substrate can be attributed to the well-established barrier protection, labyrinth effect, enhanced adhesion and interactions, as well as the presence of zinc in the LDH array. These mechanisms work synergistically to prevent the permeation of corrosive substances, improve adhesion to the steel substrate, and enhance the overall protective performance of the coating.

4. Conclusion

In conclusion, our study demonstrates the remarkable potential of incorporating layered double hydroxide (LDH) fillers into polymeric PVDF coatings for enhancing the corrosion resistance of mild steel in NaCl solutions. Our investigation successfully confirmed the synthesis of

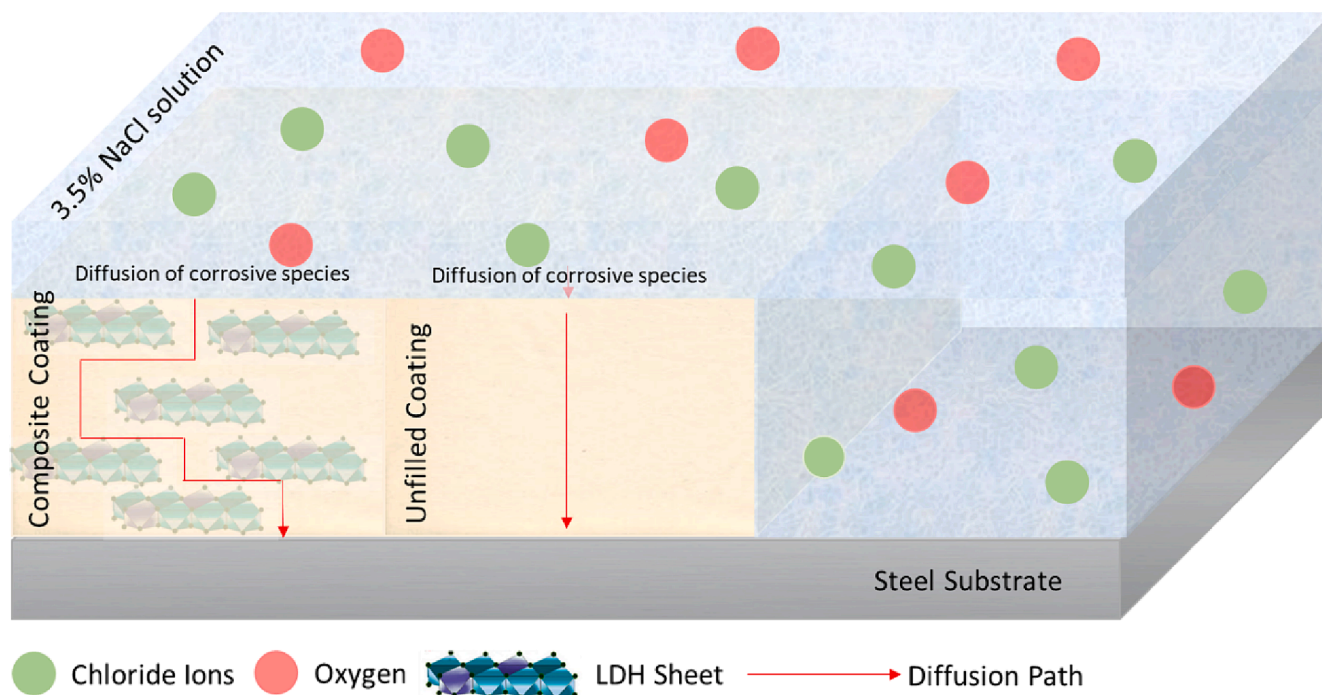


Fig. 19. Schematic diagram of coating protection mechanism.

LDH composites using a combined co-precipitation and hydrothermal process, employing various characterization techniques such as XRD, FTIR, morphological analysis, and elemental mapping.

- The introduction of LDH composites into the coatings yielded a substantial improvement in surface characteristics. These enhancements included a more uniform and smoother surface texture, the elimination of the porous structure, and the promotion of robust bonding with PVDF.
- The LDH@PVDF composite coatings with the thickness of $40 \pm 2 \mu\text{m}$ exhibited superior adhesion forces and interfacial adhesion with the steel substrate, ensuring long-term anti-corrosion performance.
- Additionally, the incorporation of LDH composites conferred hydrophobic properties and enhanced antifouling characteristics of the coatings, further elevating their corrosion resistance.
- A comprehensive assessment of corrosion resistance through measurements of open circuit potential (OCP), potentiodynamic polarization (PDP), and electrochemical impedance spectroscopy (EIS) conclusively demonstrated the outstanding performance of LDH@PVDF coatings when compared to neat PVDF coatings.
- Among the LDH composites examined, the ZLDH@PVDF coating emerged as the top-performing option, showcasing the highest level of corrosion resistance, thus emphasizing its potential for long-term corrosion protection.
- In-depth insights into the long-term corrosion behavior of the coated samples were provided by EIS measurements, which revealed that the ZLDH@PVDF coating maintained a highly efficient protective layer without undergoing diffusion-controlled electrochemical processes.
- The study provided a comprehensive exploration of the underlying mechanisms governing the performance of ZLDH@PVDF coated steel samples.

CRedit authorship contribution statement

Jwahr M. AlGhamdi: Conceptualization, Data curation, Formal analysis, Investigation, Methodology, Resources, Supervision, Visualization, Writing – original draft, Writing – review & editing. **Hissah A. Alqatani:** Conceptualization, Data curation, Investigation, Methodology, Visualization, Writing – original draft. **Nuhu Dalhat Mu'azu:** Conceptualization, Data curation, Investigation, Resources, Supervision, Validation, Writing – review & editing. **Mukarram Zubair:** Formal analysis, Writing – original draft. **Shamsuddeen A. Haladu:** Formal analysis, Writing – original draft. **Mohammad Saood Manzar:** Data curation, Resources.

Declaration of Competing Interest

The authors declare that they have no known competing financial interests or personal relationships that could have appeared to influence the work reported in this paper.

Acknowledgments

This research was conducted at Imam Abdulrahman Bin Faisal University (IAU), and the resources and equipment necessary for this study were provided by the university. No specific grant or external funding was received for this research. The authors express their gratitude to the BASRC at IAU for their assistance with characterizing the LDH samples.

References

Ahmad, S., Nawaz, M., Mohammad, S., Shakoor, R.A., 2023. Modified Ni-Al layer double hydroxides as nanoparticles for self-healing anti-corrosion composite coating Surface & Coatings Technology Modified Ni-Al layer double hydroxides as

- nanoparticles for self-healing anti-corrosion composite coating. Surf. Coat. Technol. 476, 130172 <https://doi.org/10.1016/j.surfcoat.2023.130172>.
- Ali, A.A., Madkour, M., Al Sagheer, F., Nazeer, A.A., 2021. Alumina lath-like structure-rGO-PVDF hybrid film formation with high-performance corrosion protection for 316L stainless-steel alloy. J. Mater. Res. Technol. 15, 3694–3707. <https://doi.org/10.1016/j.jmrt.2021.10.017>.
- Anjum, M.J., Zhao, J., Zahedi Asl, V., Yasin, G., Wang, W., Wei, S., Zhao, Z., Qamar Khan, W., 2019. In-situ intercalation of 8-hydroxyquinoline in Mg-Al LDH coating to improve the corrosion resistance of AZ31. Corros. Sci. 157, 1–10. <https://doi.org/10.1016/j.corsci.2019.05.022>.
- Bakhtaoui, N., Benali, O., Mazarío, E., Recio, F.J., Herrasti, P., 2021. Layered double hydroxides intercalated with methyl orange as a controlled-release corrosion inhibitor for iron in chloride media. Nano Express 2. <https://doi.org/10.1088/2632-959X/abe2b6>.
- Basu, D., Das, A., Stöckelhuber, K.W., Wagenknecht, U., Heinrich, G., 2014. Advances in layered double hydroxide (LDH)-based elastomer composites. Prog. Polym. Sci. 39, 594–626. <https://doi.org/10.1016/j.progpolymsci.2013.07.011>.
- Benício, L.P.F., Eulálio, D., de Moura Guimarães, L., Pinto, F.G., Da Costa, L.M., Tronto, J., 2018. Layered Double Hydroxides as Hosting Matrices for Storage and Slow Release of Phosphate Analyzed by Stirred-Flow Method. Mater. Res. 21, 20171004. <https://doi.org/10.1590/1980-5373-MR-2017-1004>.
- Cai, M., Fan, X., Yan, H., Li, Y., Song, S., Li, W., Li, H., Lu, Z., Zhu, M., 2021. In situ assemble Ti3C2Tx MXene@MgAl-LDH heterostructure towards anticorrosion and antiwear application. Chem. Eng. J. 419, 130050 <https://doi.org/10.1016/j.cej.2021.130050>.
- Cao, Y., Zheng, D., Zhang, F., Pan, J., Lin, C., 2022. Layered double hydroxide (LDH) for multi-functionalized corrosion protection of metals: A review. J. Mater. Sci. Technol. 102, 232–263. <https://doi.org/10.1016/j.jmst.2021.05.078>.
- Cavani, F., Trifirò, F., Vaccari, A., 1991. Hydrotalcite-type anionic clays: Preparation, properties and applications. Catal. Today 11, 173–301. [https://doi.org/10.1016/0920-5861\(91\)80068-K](https://doi.org/10.1016/0920-5861(91)80068-K).
- Centa, U.G., Mihel, M., 2022. The Effect of PVP on Thermal, Mechanical, and Dielectric. Chen, Y., Wu, L., Yao, W., Zhong, Z., Chen, Y., Wu, J., Pan, F., 2021. One-step in situ synthesis of graphene oxide/MgAl-layered double hydroxide coating on a micro-arc oxidation coating for enhanced corrosion protection of magnesium alloys. Surf. Coat. Technol. 413, 127083 <https://doi.org/10.1016/j.surfcoat.2021.127083>.
- Cheng, X., Xia, J., Wu, R., Jin, W., Pan, C., 2022. Optimisation of sacrificial anode cathodic protection system in chloride-contaminated reinforced concrete structure. J. Build. Eng. 45, 103515 <https://doi.org/10.1016/j.jobe.2021.103515>.
- Choong, P.S., Rusli, W., Seayad, A.M., Seayad, J., Jana, S., 2024. Crosslinked succinic acid based non-isocyanate polyurethanes for corrosion resistant protective coatings. Prog. Org. Coatings 186, 107961. <https://doi.org/10.1016/j.porgcoat.2023.107961>.
- Du, P., Qiu, S., Liu, C., Liu, G., Zhao, H., Wang, L., 2018. In situ polymerization of sulfonated polyaniline in layered double hydroxide host matrix for corrosion protection. New J. Chem. 42, 4201–4209. <https://doi.org/10.1039/c7nj05127a>.
- Ghazali, N., Basirun, W.J., Mohammed Nor, A., Johan, M.R., Abdul Rahman, F., 2023. Corrosion-resistant super-amphiphobic (PVDF-fnAl2O3) coating with thermal and mechanical stability. J. Coatings Technol. Res. <https://doi.org/10.1007/s11998-023-00840-0>.
- Gomes, C., Mir, Z., Sampaio, R., Bastos, A., Tedim, J., Maia, F., Rocha, C., Ferreira, M., 2020. Use of ZnAl-Layered Double Hydroxide (LDH) to Extend the Service Life of Reinforced Concrete. Mater. 2020, Vol. 13, Page 1769 13, 1769. Doi: 10.3390/MA13071769.
- Gu, L., Liu, S., Gu, L., Zhao, H., Chen, J., Yu, H., 2016. Corrosion Resistance of Graphene-Reinforced Waterborne Epoxy Coatings Journal of Materials Science & Technology Corrosion Resistance of Graphene-Reinforced Waterborne Epoxy Coatings. J. Mater. Sci. Technol. 32, 425–431. <https://doi.org/10.1016/j.jmst.2015.12.017>.
- Han, Y.Y., Liu, Z.L., Wang, S., Wang, W., Wang, C.X., Gao, C.H., 2021. Highly dispersed polyaniline/graphene oxide composites for corrosion protection of polyvinyl chloride/epoxy powder coatings on steel. J. Mater. Sci. 56, 12486–12505. <https://doi.org/10.1007/s10853-021-05925-y>.
- Honarvar Nazari, M., Zhang, Y., Mahmoodi, A., Xu, G., Yu, J., Wu, J., Shi, X., 2022. Nanocomposite organic coatings for corrosion protection of metals: A review of recent advances. Prog. Org. Coatings 162, 106573. <https://doi.org/10.1016/j.porgcoat.2021.106573>.
- Hu, J., Gan, M., Ma, L., Li, Z., Yan, J., Zhang, J., 2014. Synthesis and anticorrosive properties of polymer-clay nanocomposites via chemical grafting of polyaniline onto Zn-Al layered double hydroxides. Surf. Coat. Technol. 240, 55–62. <https://doi.org/10.1016/j.surfcoat.2013.12.012>.
- Imanieh, I., Afshar, A., 2019. Corrosion protection of aluminum by smart coatings containing layered double hydroxide (LDH) nanocontainers. Integr. Med. Res. 8, 3004–3023. <https://doi.org/10.1016/j.jmrt.2018.05.030>.
- Iqbal, M.A., Fedel, M., 2019. Effect of synthesis conditions on the controlled growth of MgAl-LDH corrosion resistance film: Structure and corrosion resistance properties. Coatings 9. <https://doi.org/10.3390/coatings9010030>.
- Iqbal, M.A., Sun, L., Barrett, A.T., Fedel, M., 2020. Layered Double Hydroxide Protective Films Developed on Aluminum and Aluminum Alloys: Synthetic Methods and Anti-Corrosion Mechanisms. Coatings. <https://doi.org/10.3390/coatings10040428>.
- Isakhani-Zakaria, M., Allahkaram, S.R., Ramezani-Varzaneh, H.A., 2019. Evaluation of corrosion behaviour of Pb-Co3O4 electrodeposited coating using EIS method. Corros. Sci. 157, 472–480. <https://doi.org/10.1016/j.corsci.2019.06.023>.
- Jiang, Y., Gao, S., Liu, Y., Huangfu, H., Guo, X., Zhang, J., 2022. Surface & Coatings Technology Enhancement of corrosion resistance of AZ31B magnesium alloy by preparing MgAl-LDHs coatings modified with imidazolium based dicationic ionic liquids. Surf. Coat. Technol. 440, 128504 <https://doi.org/10.1016/j.surfcoat.2022.128504>.

- Jin, Y., Chen, Z., Yang, W., Yin, X., Chen, Y., Liu, Y., 2020. Electrosynthesis of molybdate-doped P(ANI-co-PY) copolymer coating in ionic liquid for corrosion protection of 304 stainless steel. *J. Taiwan Inst. Chem. Eng.* 117, 171–181. <https://doi.org/10.1016/j.jtice.2020.11.027>.
- Kartsonakis, I.A., 2021. Special issue on “advances in organic corrosion inhibitors and protective coatings”. *Appl. Sci.* 11, 1–4. <https://doi.org/10.3390/app11010123>.
- Khitous, M., Salem, Z., Halliche, D., 2015. Removal of phosphate from industrial wastewater using uncalcined MgAl-NO₃ layered double hydroxide: batch study and modeling. *New pub Balaban* 57, 15920–15931. <https://doi.org/10.1080/19443994.2015.1077745>.
- Klopprogge, J.T., Hickey, L., Frost, R.L., 2004. FT-Raman and FT-IR spectroscopic study of synthetic Mg/Zn/Al-hydroxalicates. *J. Raman Spectrosc.* 35, 967–974. <https://doi.org/10.1002/JRS.1244>.
- Li, Z., Wang, X., Zhang, Y., Jing, C., 2018. Enhancing the Corrosion Resistance of Epoxy Coatings by Impregnation with a Reduced Graphene Oxide-Hydrophobic Ionic Liquid Composite. *ChemElectroChem* 5, 3300–3306. <https://doi.org/10.1002/celec.201800725>.
- Lin, K., Luo, X., Pan, X., Zhang, C., Liu, Y., 2019. Enhanced corrosion resistance of LiAl-layered double hydroxide (LDH) coating modified with a Schiff base salt on aluminum alloy by one step in-situ synthesis at low temperature. *Appl. Surf. Sci.* 463, 1085–1096. <https://doi.org/10.1016/j.apsusc.2018.09.034>.
- Liu, A., Tian, H., Li, W., Wang, W., Gao, X., Han, P., Ding, R., 2018. Delamination and self-assembly of layered double hydroxides for enhanced loading capacity and corrosion protection performance. *Appl. Surf. Sci.* 462, 175–186. <https://doi.org/10.1016/j.apsusc.2018.08.109>.
- Liu, Y., Yu, T., Cai, R., Li, Y., Yang, W., Caro, J., 2015. One-pot synthesis of NiAl-CO₃ LDH anti-corrosion coatings from CO₂-saturated precursors. *RSC Adv.* 5, 29552–29557. <https://doi.org/10.1039/c5ra01969a>.
- Liu, P., Zhang, Y., Liu, S., Zhang, Y., Qu, L., 2019. Fabrication of superhydrophobic marigold shape LDH films on stainless steel meshes via in-situ growth for enhanced anti-corrosion and high efficiency oil-water separation. *Appl. Clay Sci.* 182, 105292. <https://doi.org/10.1016/j.clay.2019.105292>.
- Luo, Z.-G., Zhang, Y., Wang, H., Wan, S., Song, L.-F., Liao, B.-K., Guo, X.-P., 2024. Modified nano-lignin as a novel biomass-derived corrosion inhibitor for enhanced corrosion resistance of carbon steel. *Corros. Sci.* 227, 111705. <https://doi.org/10.1016/j.corsci.2023.111705>.
- Mikhailau, A., Maltanova, H., Poznyak, S.K., Salak, A.N., Zheludkevich, M.L., Yasakau, K. A., Ferreira, M.G.S., 2019. One-step synthesis and growth mechanism of nitrate intercalated ZnAl LDH conversion coatings on zinc. *Chem. Commun.* 55, 6878–6881. <https://doi.org/10.1039/C9CC02571E>.
- Mochane, M.J., Magagula, S.I., Sefadi, J.S., Sadiku, E.R., Mokhena, T.C., 2020. Morphology, thermal stability, and flammability properties of polymer-layered double hydroxide (Ldh) nanocomposites: A review. *Crystals* 10, 1–26. <https://doi.org/10.3390/cryst10070612>.
- Mohamed, A.M.A., Abdullah, A.M., Younan, N.A., 2015. Corrosion behavior of superhydrophobic surfaces: A review. *Arab. J. Chem.* 8, 749–765. <https://doi.org/10.1016/j.arabjc.2014.03.006>.
- Mohammadkhani, R., Ramezanzadeh, M., Saadatmandi, S., Ramezanzadeh, B., 2020. Designing a dual-functional epoxy composite system with self-healing/barrier anti-corrosion performance using graphene oxide nano-scale platforms decorated with zinc doped-conductive polypyrrole nanoparticles with great environmental stability and non-tox. *Chem. Eng. J.* 382, 122819. <https://doi.org/10.1016/j.cej.2019.122819>.
- Montemor, M.F., 2014. Functional and smart coatings for corrosion protection: A review of recent advances. *Surf. Coatings Technol.* 258, 17–37. <https://doi.org/10.1016/j.surfcoat.2014.06.031>.
- Mroczkowska, K.M., Dzienny, P., Budnicki, A., Antończak, A.J., 2021. Corrosion resistance of aisi 304 stainless steel modified both femto-and nanosecond lasers. *Coatings* 11, 1–12. <https://doi.org/10.3390/coatings11050592>.
- Muthuraman, G., Choi, Y., Daekeun, K., Hu, J., Zhang, C., Liu, A.C.L., Zhang, N., Li, J., Bakhtaoui, N., Benali, O., Mazarío, E., Recio, F.J., Herrasti, P., 2021. Layered double hydroxides intercalated with methyl orange as a controlled-release corrosion inhibitor for iron in chloride media. *Nano Express* 2, 010017. <https://doi.org/10.1088/2632-959X/ABE2B6>.
- Online, V.A., Xiao, Y., Ji, W., Chang, K., Hsu, K., Yeh, J., Liu, W., 2017. *RSC Advances* 33829–33836. Doi: 10.1039/c7ra05674e.
- Poss, F., Copolymer, A., Liu, M., Zhang, X., Wang, D., Cheng, J., Pang, X., Qu, W., n.d. Facile Fabrication of Superhydrophobic Surface from.
- Qian, Z., Liu, Z., Wang, S., Ye, X., 2021. applied sciences A Durable PVDF / PFOTES-SiO₂ Superhydrophobic Coating on AZ31B Mg Alloy with Enhanced Abrasion Resistance Performance and Anti-Corrosion Properties.
- Quispe-Dominguez, R., Naseem, S., Leuteritz, A., Kuehnert, I., 2019. Synthesis and characterization of MgAl-DBS LDH/PLA composite by sonication-assisted masterbatch (SAM) melt mixing method. *RSC Adv.* 9, 658–667. <https://doi.org/10.1039/c8ra08780f>.
- Ren, S., Meng, F., Li, X., Cui, Y., Liu, R., Liu, Y., Hu, X., Liu, L., Wang, F., 2023. A self-healing epoxy composite coating based on pH-responsive PCN-222 smart containers for long-term anticorrosion of aluminum alloy. *Corros. Sci.* 221, 111318. <https://doi.org/10.1016/j.corsci.2023.111318>.
- Sarigamala, K.K., Shukla, S., Struck, A., Saxena, S., 2019. Rationally engineered 3D-dendritic cell-like morphologies of LDH nanostructures using graphene-based core-shell structures. *Microsystems Nanoeng.* 5, 1–9. <https://doi.org/10.1038/s41378-019-0114-x>.
- Shen, X., Wang, J., Xin, G., 2021. Effect of the Zeta Potential on the Corrosion Resistance of Electroless Nickel and PVDF Composite Layers Using Surfactants. *ACS Omega* 6, 33122–33129. <https://doi.org/10.1021/acsomega.1c05490>.
- Su, Y., Qiu, S., Yang, D., Liu, S., Zhao, H., Wang, L., 2020. Active anti-corrosion of epoxy coating by nitrite ions intercalated MgAl LDH. *J. Hazard. Mater.* 391, 122215. <https://doi.org/10.1016/j.jhazmat.2020.122215>.
- Sun, B., Liu, Q., Gao, Y., Han, L., Zhang, R., Zhang, C., Jia, X., 2023. Industrial Chemistry & Materials polyethylene nanocomposites with better anti-. <https://doi.org/10.1039/d3im00031a>.
- Tedim, J., Poznyak, S.K., Kuznetsova, A., Raps, D., Hack, T., Zheludkevich, M.L., Ferreira, M.G.S., 2010. Enhancement of active corrosion protection via combination of inhibitor-loaded nanocontainers. *ACS Appl. Mater. Interfaces* 2, 1528–1535. <https://doi.org/10.1021/am100174t>.
- Tedim, J., Kuznetsova, A., Salak, A.N., Montemor, F., Snihirova, D., Pilz, M., Zheludkevich, M.L., Ferreira, M.G.S., 2012. Zn-Al layered double hydroxides as chloride nanotrans in active protective coatings. *Corros. Sci.* 55, 1–4. <https://doi.org/10.1016/j.corsci.2011.10.003>.
- Vicente, A., Rivero, P.J., Palacio, J.F., Rodríguez, R., 2021. The role of the fiber/bead hierarchical microstructure on the properties of pvdf coatings deposited by electrospinning. *Polymers (Basel)* 13, 1–18. <https://doi.org/10.3390/polym13030464>.
- Vieira, D.E.L., Salak, A.N., Ferreira, M.G.S., Vieira, J.M., Brett, C.M.A., 2022. Ce-substituted Mg-Al layered double hydroxides to prolong the corrosion protection lifetime of aluminium alloys. *Appl. Surf. Sci.* 573, 21–23. <https://doi.org/10.1016/j.apsusc.2021.151527>.
- Wang, X., Li, L., Xie, Z.H., Yu, G., 2018. Duplex coating combining layered double hydroxide and 8-quinolinol layers on Mg alloy for corrosion protection. *Electrochim. Acta* 283, 1845–1857. <https://doi.org/10.1016/j.electacta.2018.07.113>.
- Wen, T., Yan, R., Wang, N., Li, Y., Chen, T., Ma, H., 2020. PPA-containing layered double hydroxide (LDH) films for corrosion protection of a magnesium alloy. *Surf. Coatings Technol.* 383, 125255. <https://doi.org/10.1016/j.surfcoat.2019.125255>.
- Yasaei, M., Khakbiz, M., Ghasemi, E., Zamanian, A., 2019. Synthesis and characterization of ZnAl-NO₃(-CO₃) layered double hydroxide: A novel structure for intercalation and release of simvastatin. *Appl. Surf. Sci.* 467–468, 782–791. <https://doi.org/10.1016/j.apsusc.2018.10.202>.
- Yu, J., Wang, Q., O'Hare, D., Sun, L., 2017. Preparation of two dimensional layered double hydroxide nanosheets and their applications. *Chem. Soc. Rev.* 46, 5950–5974. <https://doi.org/10.1039/c7cs00318h>.
- Zhang, F., Liu, Z.G., Zeng, R.C., Li, S.Q., Cui, H.Z., Song, L., Han, E.H., 2014. Corrosion resistance of Mg-Al-LDH coating on magnesium alloy AZ31. *Surf. Coatings Technol.* 258, 1152–1158. <https://doi.org/10.1016/j.surfcoat.2014.07.017>.
- Zheludkevich, M.L., Poznyak, S.K., Rodrigues, L.M., Raps, D., Hack, T., Dick, L.F., Nunes, T., Ferreira, M.G.S., 2010. Active protection coatings with layered double hydroxide nanocontainers of corrosion inhibitor. *Corros. Sci.* 52, 602–611. <https://doi.org/10.1016/j.corsci.2009.10.020>.